Quaternary Science Reviews 390 (2026) 110107

Contents lists available at ScienceDirect

Quaternary Science Reviews

journal homepage: www.elsevier.com/locate/quascirev

Holocene glacier fluctuations at Eklutna Lake, Chugach Mountains, south-central Alaska

Hunter T. Allen [a,*], Darrell S. Kaufman [a], Nicholas P. McKay [a], Erik Schiefer [b], Laura J. Larocca [c], Britta J.L. Jensen [d], Matthew S.M. Bolton [d], Kathleen R. North [d], Nore Praet [e,f], Maarten Van Daele [e], Marc De Batist [e], Maurycy Żarczyński [a,g]

[a] School of Earth & Sustainability, Northern Arizona University, Flagstaff, AZ, USA
[b] Department of Geography, Planning & Recreation, Northern Arizona University, Flagstaff, AZ, USA
[c] School of Ocean Futures, Arizona State University, Tempe, AZ, USA
[d] Department of Earth and Atmospheric Sciences, University of Alberta, Edmonton, Alberta, Canada
[e] Renard Centre of Marine Geology, Ghent University, Krijgslaan 281, Ghent, Belgium
[f] Flanders Marine Institute (VLIZ), InnovOcean Campus, Jacobsenstraat 1, Ostend, Belgium
[g] Department of Geomorphology and Quaternary Geology, Faculty of Oceanography and Geography, University of Gdansk, Gdansk, 80309, Poland

ARTICLE INFO

Handling editor: Prof B Davies

Keywords:
Holocene
Alaska
Paleolimnology
Proglacial lakes
Rock flour
Glacier fluctuations
Tephra

ABSTRACT

Eklutna Lake, an ice-distal proglacial lake in the Chugach Mountains of south-central Alaska, preserves a continuous record of Holocene glacier fluctuations. We present a 9.6 kyr (11.15 m long) multi-proxy sediment record that integrates grain size, geochemistry, and productivity indicators to reconstruct glacier variability. The age model was constrained by radiocarbon, event markers, and tephrochronology. Most tephras were sourced from Redoubt Volcano, and two new tephras are documented here. The various indicators do not always fluctuate synchronously, reflecting sensitivity to different glacier–climate processes. Nonetheless, principal component analysis (PCA) isolated the primary variance in the dataset, providing a continuous reconstruction of rock flour abundance, validated against regional moraine chronologies and North Pacific paleoclimate syntheses. Comparison of PC1 with Holocene moraine age clusters from Alaska shows that the PC1 time series largely tracks periods of glacier expansion and stabilization. Grain size data, supported by end member modeling, show uniquely coarse grains during the early Holocene, which suggests lower lake levels until ~8.2 ka. Subsequently, PC1 values indicate: (1) rock flour abundance was lower than at present, and glaciers were likely absent or confined to cirques until 5.5 ka; (2) a stepwise glacier expansion beginning at 5.5 ka, reaching near-modern limits by ~4 ka; and (3) a different century-scale history of glacier fluctuations during the Common Era compared to previous varve-thickness-based glacier reconstructions from the lake. This record demonstrates how ice-distal proglacial lakes can provide a robust reconstruction of Holocene glacier variability, improving our understanding of glacier–climate linkages in south-central Alaska.

1. Introduction

Past glacier fluctuations are a valuable paleoclimate proxy because glacier extent is controlled by decadal-to millennial-scale variability in melt season (summer) temperature and accumulation season (winter) precipitation (Koerner, 2005; Oerlemans, 2005). Continuous time series of Holocene glacier fluctuations are difficult to reconstruct based on geomorphic evidence, such as moraines, trimlines, and other landscape features because they document discrete glacier positions, especially where they have been largely obliterated by relatively recent glacier advances. In Alaska, many glaciers reached their Holocene maximum extent during the Little Ice Age (LIA) (Barclay et al., 2009; Solomina et al., 2015; Kaufman et al., 2016), and these late-Holocene expansions likely eroded or buried evidence of earlier glacier extents. Consequently, geomorphic records of early and mid-Holocene glacier variability are sparse.

Sediments from glacially fed (proglacial) lakes provide continuous archives of glacier variability (Karlén, 1976, 1981; Noon et al., 2001),

* Corresponding author. Knoles Dr, Flagstaff, AZ 86011, USA.
E-mail address: hta42@nau.edu (H.T. Allen).

https://doi.org/10.1016/j.quascirev.2026.110107
Received 23 February 2026; Received in revised form 1 June 2026; Accepted 3 June 2026
Available online 31 July 2026
0277-3791/© 2026 The Authors. Published by Elsevier Ltd. This is an open access article under the CC BY license (http://creativecommons.org/licenses/by/4.0/).

which can be reconstructed using various indicators of rock flour abundance (Nesje et al., 2000; Bakke et al., 2005a; Røthe et al., 2015). Rock flour is generated by subglacial abrasion at the ice–bed interface, creating fine silt- and clay-sized particles that are transported downstream, where they are preserved in lake sediments. Some studies integrate lake core evidence with glacial geomorphic mapping to calibrate rock flour abundance in terms of reconstructed glacier size and to infer equilibrium line altitude (ELA) shifts (Dahl et al., 2003; Bakke et al., 2005b; Larocca et al., 2020). Others track sediment yields that reflect erosion and meltwater discharge (Leemann and Niessen, 1994; Hallet et al., 1996; Leonard, 1997; Hodgkins, 1999; Balascio et al., 2015).

Similar to other mountainous regions, previous work on proglacial lakes in Alaska has primarily focused on three types of depositional settings: (1) proglacial lakes that preserve annually laminated sediments (varves) and thereby afford high-resolution time series of sediment accumulation from which discharge and climate fluctuations can be inferred (Bird et al., 2009; Loso, 2009; Boes et al., 2018; Thomas et al., 2021); (2) threshold proglacial lakes, where glaciogenic sediment enters only when a glacier advances over the catchment divide of the lake, generating a clear on-off signal (Kaufman et al., 2003; Daigle and Kaufman, 2009; LaBrecque and Kaufman, 2016); and (3) ice-distal proglacial lakes where multiproxy analyses track changes in rock flour abundance using both the glaciogenic mineral and the biological components that are influenced by the rock flour (Levy et al., 2004; McKay and Kaufman, 2009; Benson et al., 2019; McDonald and Briner, 2026). Sediment cores from this type of proglacial lake can extend back to the late glacial period, yet only four publications (excluding graduate theses) have presented multi-millennial glacier reconstructions from Alaskan proglacial lakes, despite Alaska containing nearly 40% of all glaciers across the Arctic's major glacierized regions (RGI 7.0 Consortium, 2023). The timing and geographic pattern of pre-LIA glacier fluctuations remain poorly resolved across most of Alaska, limiting our understanding of millennial-scale glacier history in the region.

Multiple studies have used principal component analysis (PCA) to interpret multi-proxy and X-ray fluorescence (XRF) data from proglacial lake sediment cores to reconstruct Holocene glacier extent, including from Svalbard and Scandinavia (Vasskog et al., 2012; Bakke et al., 2013; Wittmeier et al., 2015; Røthe et al., 2015). In these reconstructions, the underlying assumption is that glaciers, which cover a large proportion of the studied catchments, dominate clastic sedimentation in these relatively small lakes. Consequently, the principal component (PC) that explains the greatest variance, or the individual variable with the strongest PC loading, is commonly interpreted as reflecting inorganic detrital input.

In this study, we analyze a sedimentary sequence extending back ~9600 years (9.6 ka, or thousands of calibrated years before present, where present is 1950 Common Era) from proglacial Eklutna Lake, a large lake in a catchment with relatively little glacier cover. This work contrasts with the previously mentioned study areas in Svalbard and Scandinavia because the sedimentary evidence for glacier size may be obscured in this setting relative to smaller lakes in more extensively ice-covered catchments. We evaluate our reconstruction by comparing it with previously published records from Alaska-wide syntheses that summarize periods of glacier expansion and stabilization. Our analysis addresses three questions: (1) How well do the multiple biological, chemical and physical indicators of rock flour abundance correspond with each other? (2) Can PCA extract a robust rock flour abundance signal from the multi-proxy dataset as validated by other regional records of glacier change? (3) What was the extent of glaciers through the Holocene in the catchment?

2. Study site

Eklutna Lake (61.38°N, 149.04°W; 265 m a.s.l.) is among the most intensively studied lakes in Alaska. It serves as the primary water supply and generates electricity for the municipality of Anchorage, and its sedimentary infill records major earthquakes that impacted the region during the Common Era (CE) (Praet et al., 2025). The lake is situated on the leeward side of the Chugach Mountains in south-central Alaska (Fig. 1). The climate of the region is dominantly maritime (Alaska Climate Research Center; www.akclimate.org), with mean January and July temperatures of −6.8 °C and 10.8 °C, respectively, and a mean annual precipitation of 525 mm as based on measurements made in the Eklutna Lake catchment at the mid-elevation SNOTEL Site 1035 (640 m a.s.l.; US Natural Resources Conservation Service; www.usda.gov) during the last 24 years. Precipitation distribution and intensity are strongly influenced by local topography and seasonal climate. The strength and position of the Aleutian Low atmospheric pressure system modulates precipitation variability, especially during the winter (Overland et al., 1999). Spruce, birch, and aspen forests occupy lower valley bottoms and the areas near the lake; however, the catchment is largely alpine, with alder shrubs extending above the treeline.

Eklutna Lake is an ice-distal proglacial lake that occupies a steep-walled, glacially carved valley and has an elongated morphology (9 × 1.5 km; ~14 km^2) (Fig. 2). The lake comprises two major subbasins, 50 and 58 m deep, separated by a sill that appears to have been built from deltaic deposits from Yuditna Creek. Eklutna Glacier (~26 km^2 in 2015) is the largest glacier in the watershed, and its meltwater and sediment are routed through the West Fork Eklutna River (hereafter, West Fork). The East Fork Eklutna River (East Fork) catchment is lower in elevation, and its glacier cover is less relative to that of the West Fork. Together, glaciers cover 13% of the Eklutna Lake catchment, based on imagery from 2015, and the ELA of Eklutna Glacier is ~1450 m a.s.l., based on measurements from 2008 to 2015 (Sass et al., 2017). Glacial-geomorphic features formed during repeated Pleistocene glacier advances from multiple tributaries, including Bold Creek, are represented on the landscape (Updike and Ulery, 1983; Brabets, 1993; Schmoll et al., 1999); however, none of the moraines in the catchment have direct ages. Bedrock in the catchment includes the Valdez Group and the McHugh Complex, both heterogeneous mixtures of deformed marine meta-sedimentary and meta-volcanic rocks (Clark, 1973; Winkler, 1992). Valdez Group rocks are meta-siltstones and meta-mudstones (flysch) (Winkler, 1992), while the McHugh Complex rocks are predominantly meta-clastic silt-to sandstone (Clark, 1973).

Previous work at Eklutna Lake has established hydrological, glaciological, and sedimentological framework used for interpreting late Holocene environmental change in the watershed. Surficial mapping of the catchment, combined with hydrological investigations by Brabets (1993), quantified water and sediment fluxes and documented correlations between discharge variability and suspended sediment transport from the West Fork and East Fork. Glacier mass balance monitoring of Eklutna Glacier demonstrated sustained negative mass balance and progressive thinning since the mid-20th century (Sass et al., 2017; Geck et al., 2021). Sedimentological work by Boes et al. (2018) used a multi-lake framework, including Eklutna Lake, to show that while regional climate drives multi-decadal trends in varve thickness (e.g., thicker varves during the LIA), catchment-scale geomorphology and human modifications create site-specific variations to varve structure and thickness. Fortin et al. (2019) developed a ~2.3 ka Bayesian varve chronology for Eklutna Lake, enabling a long-term reconstruction of glacier fluctuations (Thomas et al., 2021). Seismic reflection surveys identified landslide and mass-transport deposits within the basin, establishing Eklutna Lake as an archive of prehistoric earthquakes (Praet et al., 2017). Building on these datasets, sedimentological and statistical approaches were developed to distinguish between earthquake-triggered and flood-induced turbidites (Praet et al., 2020; Vandekerkhove et al., 2020). Spatial analyses of sediment cores across the lake basin (Schiefer et al., 2021) demonstrated that sediment thickness patterns in the lake reflect depositional gradients controlled by inflow proximity, basin morphology, and event-specific dispersion processes. No previous study has reported the longest sedimentary sequence yet obtained from the lake, which is the focus of this study.

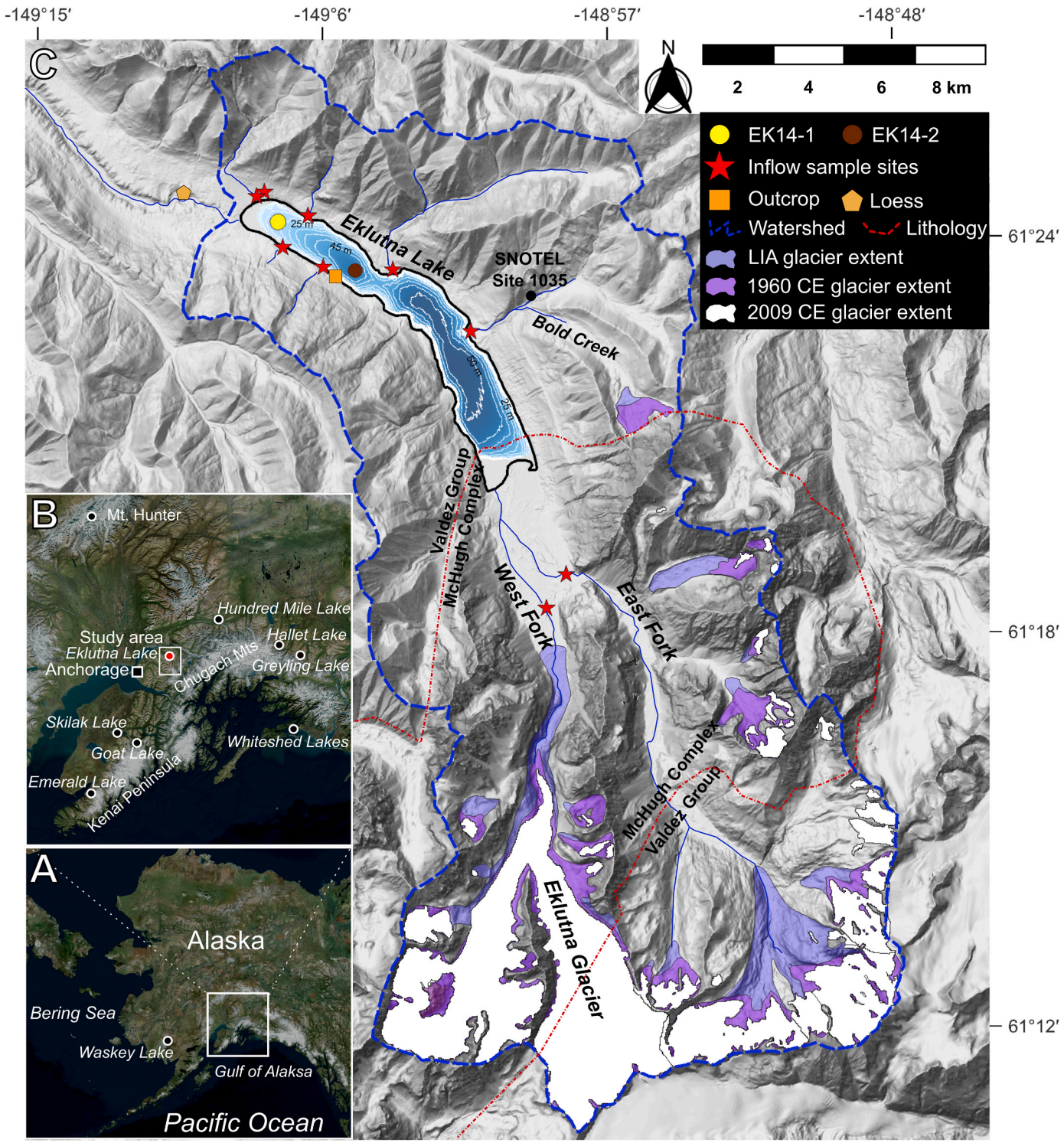


Fig. 1. Eklutna Lake catchment. (**A, B**) Inset maps of Alaska with locations of sites mentioned in this study. (**C**) Regional digital elevation model (DEM) hillshade (Porter et al., 2023). Eklutna Lake bathymetry (Haeussler et al., 2022) based on a multibeam survey conducted when the water elevation was 258 m a.s.l. The first white contour is at 5 m depth. Sampled locations in this study include lake cores (circles), inflow streams (red stars), a loess deposit (orange pentagon), and an outcrop (orange square). The contact (red dotted line) between the Valdez Group and McHugh Complex is from Clark and Bartsch (1971). Modern glacier extents based on the Randolf Glacier Atlas version 7.0 (RGI 7.0 Consortium, 2023) and Little Ice Age (LIA) extents are indicated (Brabets, 1993).

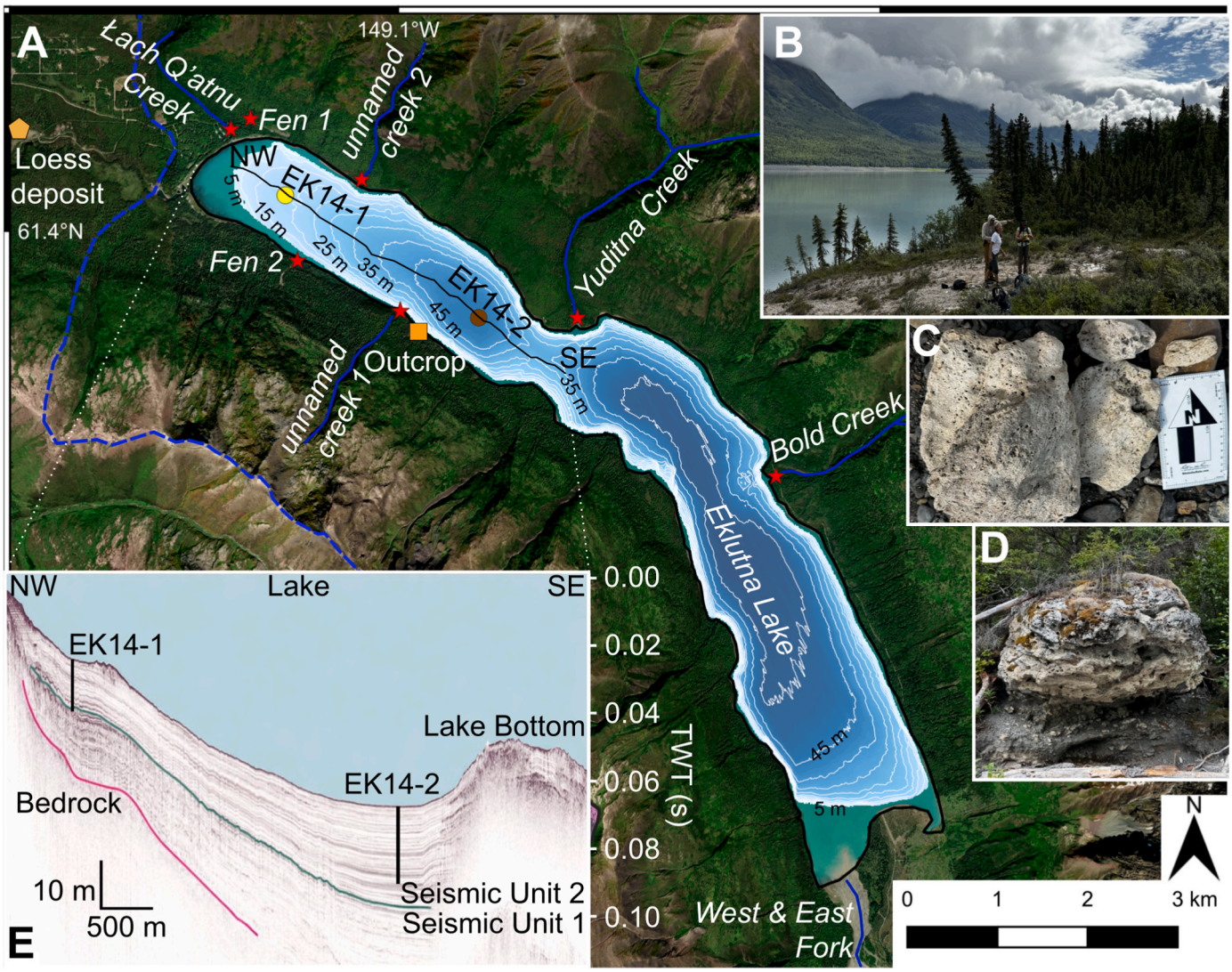


Fig. 2. Study area. (**A**) Bathymetric map of Eklutna Lake with locations mentioned in this study. (**B**) Surface of the calcareous Fen 2. (**C**) Tufa clasts found along the northwest shoreline. (**D**) Tufa boulder (3.0 × 7.0 m) found along the northwest shoreline. (**E**) Acoustic profile (NW-SE) through the distal basin showing the location of core sites (Praet et al., 2017, 2020).

3. Methods

3.1. Sediment core collection and characterization

A transect of sediment cores was retrieved from Eklutna Lake by the Renard Centre of Marine Geology (Ghent University, Belgium) in February–March 2014 using a UWITEC piston corer and platform operated on the lake ice. The primary core analyzed in this study is from the distalmost site in 21 m water depth when lake level was at approximately 259 m asl (Fig. 2). It spans 11.15 m below the lake floor and is constructed from 11 core sections taken from three nearby holes centered on 61.40334°N, −149.12414°W and referred to collectively as core EK14-1 (Appendix A). The composite core and depth scale were assembled by correlating visual stratigraphy and magnetic susceptibility (MS) profiles. Prior to splitting, whole cores were measured for wet bulk density (WBD) via gamma-ray attenuation at 0.5 cm resolution on a Geotek Multi-Sensor Core Logger at the Continental Scientific Drilling (CSD) Facility, University of Minnesota. The cores were split, sealed in several layers of plastic wrap, and refrigerated. Split core surfaces were imaged with a Geotek Core Imaging System, and MS was logged with a Bartington MS2E surface probe on a Geotek MSCL-XYZ at 0.5 cm resolution.

Geochemical data were collected on an ITRAX XRF core scanner at CSD. XRF scans were conducted at 0.5 cm resolution using a chromium tube operated at 30 kV and 55 mA with a dwell time of 15 s. To help account for matrix effects while addressing data-closure artifacts, elemental XRF count data from EK14-1 were transformed using a central log-ratio (CLR) transformation (Aitchison, 1982) to address compositional constraints (Eq. (1)); (Weltje et al., 2015; Bertrand et al., 2024).

$$W_{z,i} = ln\, W_{z,i} - \frac{1}{n}\sum_{j=1}^{n} lnW_{zj} \qquad \text{Eq. (1)}$$

In Eq. (1), $W_{z,i}$ is the number of counts for element i measured by the ITRAX core scanner at depth z. Term j corresponds to the logarithm of the geometrical mean of all elements taken at the same depth, computed by excluding elements with <500 counts averages. In addition to downcore XRF, we aimed to isolate geochemical fingerprints from the two primary glaciated tributaries, the West Fork and East Fork. To do this, we analyzed their sediment, along with sediment from non-glaciated inflow streams, for major-element composition using the same XRF methods to compare with the downcore data. Samples from each of nine inflows and one loess exposure (Fig. 2) were taken in triplicate within ~200 m of each other, and the three results were

averaged for each site (Appendix A Table A3). In the field, we collected fine-grained overbank and channel deposits, which were sieved to remove grains >63 μm. Because the XRF data are from spot samples rather than downcore scans, we relied on elemental ratios to distinguish the composition of the West Fork and East Fork sediment from that of other non-glaciated inflows.

Hyperspectral reflectance data were collected using a Specim Photonfocus MV1-D1312-C020-160 camera over the 400–1000 nm range, with a spectral resolution of approximately 1.5 nm. Data were processed according to the Butz et al. (2015) standard procedure and were scaled to a 90 μm resolution. The relative absorption band depth (RABD) between 660 and 670 nm ($RABD_{660;670}$) was calculated (Eq. (2); Rein and Sirocko, 2002) as follows:

$$RABD_{660;670} = \frac{\left[\frac{6*R_{590}+7*R_{730}}{13}\right]}{R_{min\ (660;670)}} \quad \text{Eq. (2)}$$

Where R_{590} is reflectance at 590 nm, R_{730} is reflectance at 730 nm, and $R_{min(660;670)}$ is the minimum reflectance in the 660 to 670 nm range. $RABD_{660;670}$ yields an estimate of sedimentary chlorin abundance, the diagenetic product of chlorophyll, which has absorption maxima between 660 and 670 nm (Wolfe et al., 2006). Commonly, $RABD_{660;670}$ values are proportional to actual chlorin content (Butz et al., 2015).

Bulk sediment analyses included biogenic silica (BSi) and particle size distribution measured on contiguous samples ranging from 2 to 11 cm thick, each spanning approximately 40 years based on a preliminary age model. Loss-on-ignition (LOI) was measured separately from BSi and particle size distribution on 1-cm-thick samples distributed at intervals of 2–10 cm. We generally avoided outlier beds – instantaneous deposits associated with high-energy events – and tephra beds so that they would not be combined with background sediment. For LOI, 1 cm^3 of wet sediment was weighed for WBD, oven-dried overnight at 80 °C, weighed again for dry bulk density (DBD), combusted at 550 °C for 5 h, and reweighed to estimate the percent organic matter (OM) based on the percent mass lost-on-ignition. DBD data from the LOI procedure are available in Appendix A but were not used here, as gamma-ray-inferred WBD was measured at a finer resolution. Samples for BSi and particle size distribution were treated with 30% H_2O_2 to remove organic matter and 10% Na_2CO_3 to dissolve the BSi, which was then quantified by molybdate-blue colorimetric analysis and spectrophotometric detection (modified after Mortlock and Froelich, 1989). The residual sediment was then deflocculated in 5% sodium hexametaphosphate ($Na_6[PO_3]_6$), and grain size distributions were measured using a Beckman-Coulter LS-320 laser diffraction particle size analyzer after 30 s of ultrasonic dispersion.

3.2. Statistical analysis

Grain size distributions were analyzed using End-Member Modeling (EMM) implemented by the EMMAgeo package (Dietze and Dietze, 2019). The optimal number of end members (4) was determined by inspecting the total variance explained (R^2) elbow plot. The model was run with an Oblimin rotation and a sparsity factor of $\lambda = 0.005$, with non-negative constraints applied to end member loadings and scores.

Downcore correlations among sediment properties were evaluated using Pearson correlation and non-parametric isospectral methods. Time-series data were binned into 100-year intervals, producing 96 evenly spaced values per variable (McKay et al., 2021). To account for temporal autocorrelation, we calculated statistical significance using a phase-randomized Monte Carlo approach ($n = 1000$). This method generates isospectral surrogates that preserve the original power spectrum of the time series while randomizing the phases (Ebisuzaki, 1997).

A probabilistic principal component analysis (pPCA; Tipping and Bishop, 1999) was performed on eight downcore bulk sediment properties binned at 2 cm resolution using the geoChronR package (McKay et al., 2021). Selected properties include: OM, BSi, $RABD_{660;670}$, WBD, sedimentation rate, particle-size endmember 1 (EM1), median grain size (D50), and the ratio of silicon to aluminum (Si/Al), and are each discussed in their relation to rock flour abundance in Section 5.1. A pPCA was used because of differences in the sampling density across datasets, as it uses an expectation maximization algorithm to iteratively infill missing data (Stacklies et al., 2007; McKay et al., 2021).

3.3. Geochronology

Radiocarbon (^{14}C) ages were analyzed by a Mini Carbon Dating System (MICADAS) at the Arizona Climate and Ecosystems (ACE) Isotope Lab, Northern Arizona University. Approximately 0.1–0.3 mg of macrofossils were collected from targeted downcore intervals. Macrofossil fragments, including various identifiable and unidentifiable plant fragments, were hand-picked. Samples (<0.3 mg) were treated with weak acid (Zander et al., 2020) and injected onto the MICADAS using a Gas Interface System (GIS), except one large sample (ACE-690.1.1), which was processed with a strong acid-base-acid treatment (Olsson, 1986) and converted to graphite. Snails collected from an outcrop (Appendix A Section A2) and the modern shoreline were cleaned by leaching approximately 30% of their mass, then injected onto the MICADAS using the GIS. For reporting, all radiocarbon ages were calibrated using CALIB 7.0 (Stuiver and Reimer, 1993) and the IntCal20 calibration curve (Reimer et al., 2020) (Table 2). Calibrated ages are reported as the median of the probability distribution, with 95% confidence intervals. All ages are given in calendar years before present (cal yr BP) or in thousands of calendar years (ka).

Sampling and preparation of tephra samples for geochemical analyses followed the methods of Praet et al. (2022). The major element composition of individual glass shards were measured using wavelength-dispersive spectrometry on a JEOL 8900 electron microprobe at the University of Alberta. The instrument was operated with an accelerating voltage of 15 keV, a beam current of 6 nA, and a beam diameter of 5 μm. To account for potential Na loss, time-dependent intensity corrections were applied using the software "Probe for EPMA" (Donovan et al., 2015; Jensen et al., 2021). Standard reference materials (Lipari rhyolitic obsidian (ID 3506) and Old Crow tephra (Kuehn et al., 2011)) were analyzed alongside all samples to ensure proper calibration. Averages and standard deviations of key tephra samples are summarized in Appendix A Table A1, while all point-by-point data for the samples and standards are available in Appendix A.

4. Results

4.1. Stratigraphy

4.1.1. Seismic stratigraphy

Geoacoustic sub-bottom data were acquired in 2012 using a 3.5 kHz GEOPULSE pinger source mounted on an inflatable cataraft. Praet et al. (2017) describe the post-processing and analysis of several transects. Here, we focus on a single NW-SE profile that runs through the distal basin of the lake and the EK14-1 coring site (Fig. 2E). Core EK14-1 penetrates roughly half of the lake infill at the coring location. The sub-bottom profile shows two main seismic units (Seismic Units 1 and 2)

Table 1
Tephra analyzed for glass geochemistry from core EK14-1.

Lab ID (UA-)[a]	Core EK14-1-	Eklutna Tephra Identifier	Bottom Depth blf (cm)	Thickness (cm)	Age (cal yr BP)	± (yr)[b]	Compositional Type	Basis of Age	Reference
4245	1C-1U-1	EK-T5	141.5	0.5	446	24	Redoubt	Varves	Praet et al. (2025)
4378	1D-1U-1	EK-T10	336.0	1.0	1287	53	Redoubt	Varves	Praet et al. (2025)
4246	1D-1U-2	EK-T12	437.5	1.0	1723	96	Redoubt	Varves	Praet et al. (2025)
4247	1C-2U-2	EK-T17	599.5	2.0	2788	325	Redoubt	^{14}C age model	This study
3073	1D-2U-1	EK-T18	747.0	1.0	3713	144	Hayes Tephra H2	Tephra correlation	Bolton et al. (2020)
4379/4465	1C-3U-1	EK-T18b	927.5	1.0	6226	252	Redoubt	^{14}C age model	This study
4248	1C-3U-2	EK-T19	940.0	1.0	6430	38	Oshetna-Redoubt	Tephra correlation	Davies et al. (2024)
4466	1C-3U-2	EK-T20	975.5	1.0	7032	313	Augustine	^{14}C age model	This study

[a] Tephra samples were analyzed at the University of Alberta by the Volcanic Ash Research Group.
[b] One-half of 95% confidence interval.

Table 2
Radiocarbon and marker bed ages from core EK14-1.

Lab ID (ACE)[a]	Core EK14-1-	Composite Depth (cm)[b]	Weight (μg C)	^{14}C Age (yr)	± (yr)	Material Dated or Correlated Bed	Median Age (cal yr BP)[c]	95% CI Min. (cal yr BP)	95% CI Max. (cal yr BP)
-	1C-1U-1	18.0	-	-	-	1964 CE EQ	−14	-	-
	1C-1U-1	26.5	-	-	-	1929 CE dam failure	25	-	-
-	1C-1U-1	30.0	-	-	-	1916 CE flood turbidite	34	-	-
6336.1.1	1C-1U-1	79.0	44	398	63	Leaves	438	313	525
6337.1.1*	1D-1U-2	380.5	97	2102	70	Numerous *Drepanocladus* leaves	2074	1887	2308
6338.1.1*	1D-1U-2	382.0	40	2235	77	Moss stems, leaves, insect legs, twig	2224	2149	2273
6339.1.1*	1C-2U-1	542.0	22	3169	82	Seed, *Drepanocladus* stem, charcoal, beetle chitin	3383	3255	3566
1749.1.1	1D-2U-2	862.0	97	4315	105	Wood	4918	4651	5286
1747.1.1	1C-3U-1	944.5	99	5440	118	Bryophyte twigs	6218	6009	6446
3220.1.1	1C-3U-2	990.5	97	6417	75	Unidentifiable plants	7737	7275	7469
690.1.1*	1C-3U-2	1018.0	249	7635	19	Partly burned wood	8412	8394	8452
6341.1.2	1C-3U-2	1044.5	56	7113	93	Insect and *Chladocera* chitin, terrestrial leaves	7930	7843	8168
6342.1.1	1C-3U-2	1047.0	92	7254	93	Moss stems, leaves, insect chitin	8081	7980	8318
1748.1.1	1C-3U-2	1083.0	85	8032	146	Bryophyte twigs	8902	8642	9401
3221.1.1	1C-3U-2	1113.0	50	8642	94	Unidentifiable plants	9647	9530	10111

* Samples excluded from the age-depth model.
[a] Samples were analyzed at the ACE Isotope Laboratory at Northern Arizona University using the Gas Interface System of the MICADS, except for ACE 690.1.1, which was analyzed using graphite.
[b] Composite depth is the mid depth below lake surface of a 1- to 5-cm-thick sample.
[c] ^{14}C ages were calibrated to calendar years before present (cal yr BP; 1950) using CALIB 8.2 (Stuiver and Reimer, 1993) and IntCal20 (Reimer et al., 2020), and tephra ages are from previous work as specified in the text.

with their boundary around 10.5 m blf near core EK14-1 (Fig. 2E). In the depocenter of the distal subbasin, both units have continuously stratified seismic facies with mostly low-amplitude reflections driven by minor velocity-density contrasts. In the shallower areas of the distal subbasin near core EK14-1, the seismic facies in Seismic Unit 2 (i.e., the upper unit) still show continuous low-amplitude reflections, albeit in a condensed section, while the reflections in Seismic Unit 1 (i.e., the lower unit) become higher in amplitude and more irregular to chaotic. Moreover, around the unit boundary, the onlap terminations – indicating the shoreline position (Vail et al., 1977) – abruptly become shallower at the onset of Seismic Unit 2, resembling a transgressive surface, and shifting in total about ~15 m vertically.

Using an acoustic velocity of 1500 m s^{-1} (Praet et al., 2022), core EK14-1 penetrates the entire Seismic Unit 2, as well as ~0.6 m of the lower seismic unit. Furthermore, assuming a slightly higher acoustic velocity of 1600 m s^{-1} for the high-amplitude reflections of Seismic Unit 1, we estimate the base of core EK14-1 to be about 14 m above the base of the acoustically stratified section. Consequently, the core did not capture the onset of deglaciation in the catchment, which probably occurred several millennia earlier. An end moraine at the lake outlet has been correlated with the regional Elmendorf Stade (Schmoll et al., 1999), which is dated to ~17.3 ± 1.5 ka in the Chugach Mountains (Valentino et al., 2021); the deglaciation of Eklutna Lake began sometime after.

4.1.2. Unit descriptions

The sedimentary sequence in EK14-1 is divided into three main stratigraphic units (Figs. 3 and 4; Table 3). At the macroscopic scale, colors and textures are gradational with depth, making it somewhat arbitrary to distinguish units; therefore, shifts in measured properties are used to delimit unit boundaries. Relatively low accumulation rates explain the discontinuous and indistinct varves, which preclude a varve-based chronology unlike those captured at other sites in Eklutna Lake (Fortin et al., 2019; Thomas et al., 2021). Unit 1 (11.15–10.61 m; 9.6–8.2 ka) consists of dark brown coarse silt (Munsell 10 YR 3/3) with black (10 YR 2/1) interbeds and distinctly coarser grains than in overlying units. A fining upward, 2-cm-thick dark grey bed at 10.61 m marks the transition to Unit 2, above which particle sizes are finer. Unit 2 (10.61–7.47 m; 8.2–3.7 ka) is composed of very dark grey (2.5 YR 3/1) laminated silty clay with intermittent black (2.5 YR 2.5/1) beds. It is subdivided into subunits 2a (10.61–8.87 m; 8.2–5.5 ka) and 2b (8.87–7.47 m; 5.5–3.7 ka) based on a sharp decrease in BSi and an increase in WBD. Unit 3 (7.47–0 m: 3.7 ka–2014 CE) is silty clay and is clearly defined by its higher sedimentation rate, finer grains, and reduced OM, including chlorin. Its color transitions from greyish brown (10 YR 5/2; 7.47–6.70 m) to light yellowish brown (10 YR 6/4; 6.70 m–top), transitions to thin laminations (0.1–0.5 cm) and occasional black beds.

4.1.3. Outlier beds

Besides tephra layers, other visually distinct beds relative to surrounding sediments occur throughout core EK14-1 (Fig. 3). We call such beds thicker than 1 cm "outlier beds." They generally fall into two groups: (1) massive, silty sand layers that are black or brown, and (2) sandy-based, upward-graded layers capped by light-grey-blue clay. XRF core scanning at 0.5 cm resolution and finer show that these beds vary in

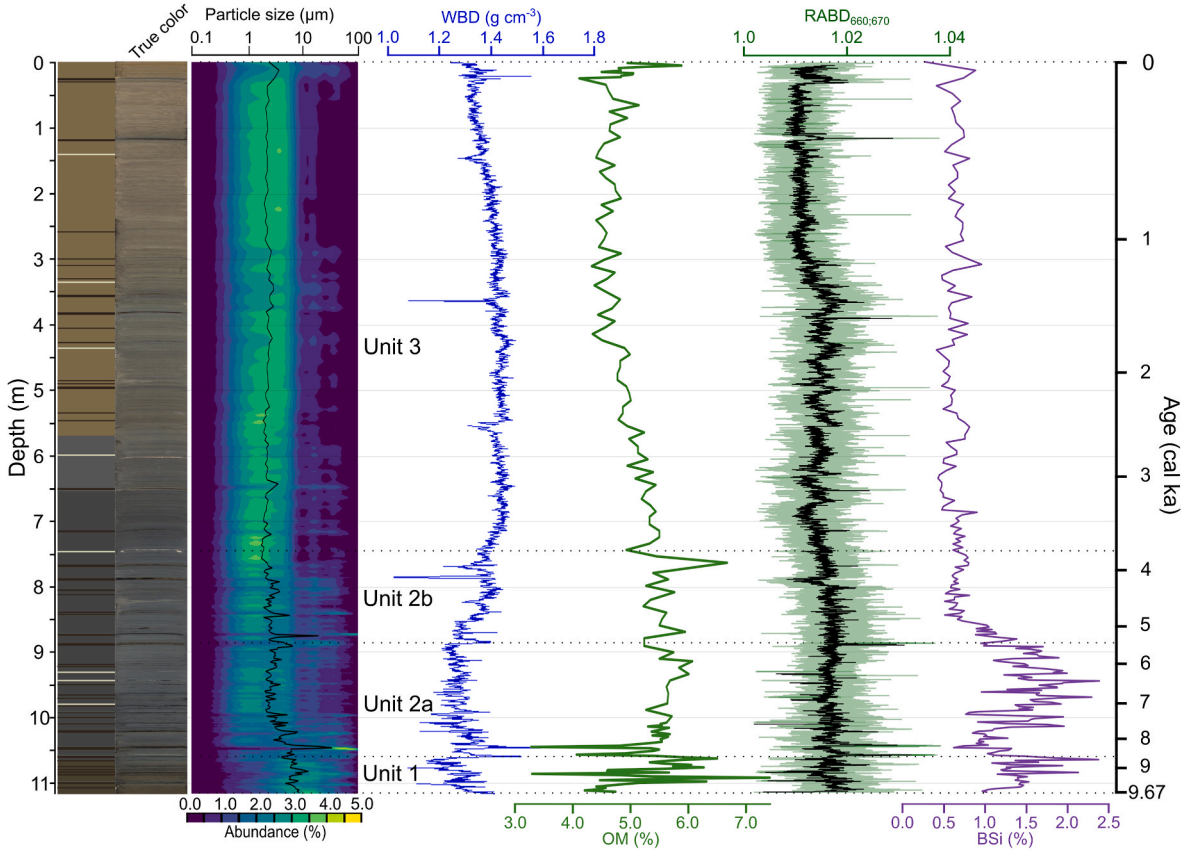


Fig. 3. Core EK14–1 selected biological and physical properties and unit boundaries plotted by depth (left y-axis) and age (right y-axis). From left to right, panels show: Lithologic log with tephras (white) and outlier beds (black). True color image of composite core. Particle size heatmap with median grain size (D50) (black line). Wet bulk density (WBD) from gamma-ray attenuation. Organic matter (OM) abundance based on loss on ignition. Total chlorin relative abundance inferred from hyperspectral imaging ($RABD_{660;670}$), with a 20-point (1.8 mm) running average (black line) overlaid. Biogenic silica (BSi) abundance.

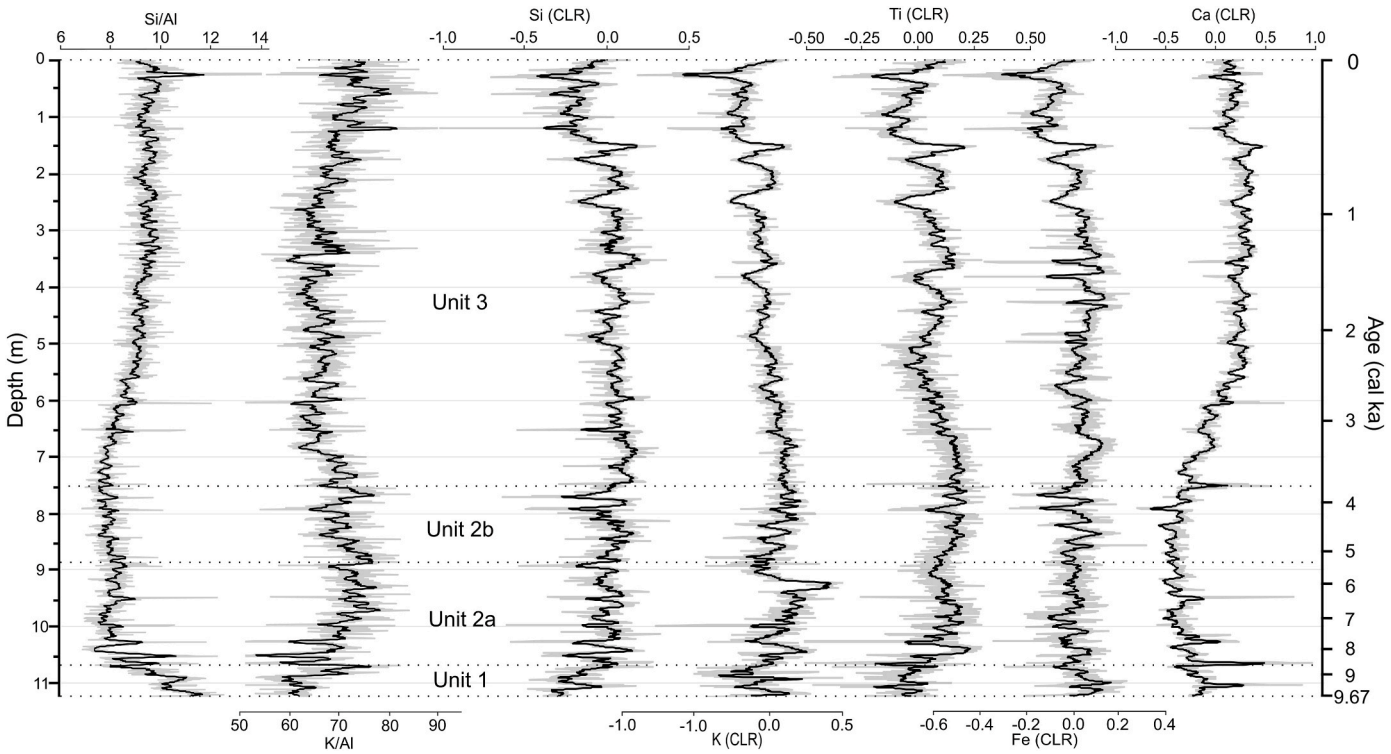


Fig. 4. Selected X-ray fluorescence (XRF) and unit boundaries plotted by depth (left y-axis) and age (right y-axis). From left to right: Si/Al and K/Al are raw count data ratios. Si, K, Ti, Fe, and Ca were converted to the central log ratio (CLR; Weltje et al., 2015; Bertrand et al., 2024). The overlaid black lines represent the 10-point (5 cm) running averages. Additional XRF data from core EK14-1 are available in Appendix A.

Table 3
Summary of average (±1 σ) sediment characteristics for each stratigraphic unit of core EK14-1. Number of measurements per average is in parentheses.

Sediment property	Unit 1	Unit 2		Unit 3
		Unit 2a	Unit 2b	
Depth (m blf)	11.15 – 10.61	10.61 – 8.87	8.87 – 7.47	7.47 – 0.0
Age range (cal ka)	9.6 – 8.2	8.2 – 5.5	5.5 – 3.7	3.7 – 0.0
Sedimentation rate (mm yr^{-1})	0.36 ± 0.12 (54)	0.06 ± 0.14 (174)	0.81 ± 0.15 (140)	2.17 ± 1.03 (747)
WBD (g cm^{-3})	1.32 ± 0.12 (110)	1.35 ± 0.07 (348)	1.43 ± 0.08 (280)	1.50 ± 0.06 (1495)
$RABD_{660;670}$	1.017 ± 0.005 (8563)	1.017 ± 0.004 (23361)	1.016 ± 0.003 (15792)	1.013 ± 0.004 (93422)
OM (%)	5.23 ± 0.83 (26)	5.55 ± 0.70 (39)	5.61 ± 0.37 (13)	4.88 ± 0.38 (84)
BSi (%)	1.42 ± 0.33 (26)	1.42 ± 0.37 (85)	0.80 ± 0.22 (51)	0.62 ± 0.11 (100)
Ca (CLR)	−0.15 ± 0.20 (108)	−0.32 ± 0.22 (348)	−0.41 ± 0.10 (279)	0.16 ± 0.19 (1491)
Si (CLR)	−0.19 ± 0.14 (108)	−0.01 ± 0.12 (348)	0.005 ± 0.14 (279)	0.001 ± 0.14 (1491)
K (CLR)	−0.09 ± 0.24 (108)	0.09 ± 0.16 (348)	0.05 ± 0.13 (279)	−0.05 ± 0.13 (1491)
Ti (CLR)	−0.06 ± 0.10 (108)	0.10 ± 0.12 (348)	0.14 ± 0.07 (279)	0.04 ± 0.10 (1491)
Fe (CLR)	0.04 ± 0.09 (108)	−0.01 ± −0.01 (348)	−0.01 ± 0.08 (279)	−0.01 ± 0.09 (1491)
Al (CLR)	−0.03 ± 0.13 (108)	0.09 ± 0.12 (348)	0.06 ± 0.12 (279)	−0.03 ± 0.18 (1491)
Si/Al	10.28 ± 0.98 (108)	8.17 ± 0.85 (348)	7.91 ± 0.52 (279)	9.06 ± 0.80 (1491)
K/Al	64.45 ± 6.23 (108)	70.76 ± 6.15 (348)	71.02 ± 4.41 (279)	67.89 ± 5.27 (1491)
$CaCO_3$ (%)	not detected (2)	not detected (4)	not detected (1)	not detected (13)
PC1	0.16 ± 0.06 (24)	0.13 ± 0.03 (82)	0.05 ± 0.04 (70)	−0.07 ± 0.04 (366)
D50 (μm)	7.85 ± 2.16 (26)	3.54 ± 3.04 (85)	3.05 ± 1.52 (51)	2.28 ± 0.33 (100)
Clay (%)	19.78 ± 4.02 (26)	38.46 ± 6.84 (85)	42.96 ± 6.79 (51)	45.33 ± 3.88 (100)
EM1 (%)	7.5 ± 8.1 (26)	44.1 ± 17.2 (85)	60.3 ± 17.9 (51)	86.6 ± 9.6 (100)
EM2 (%)	83.4 ± 8.7 (26)	28.3 ± 19.3 (85)	24.4 ± 19.8 (51)	11.8 ± 10.1 (100)
EM3 (%)	7.9 ± 11.5 (26)	23.8 ± 17.6 (85)	12.5 ± 10.6 (51)	1.5 ± 3.7 (100)

composition and can be difficult to distinguish from background sediment. In total, we identified 38 massive beds ≥1.0 cm thick and six upward-graded beds averaging ~2.5 cm thick (Fig. 3). Units 1 ($n = 6$) and 2 ($n = 20$) together have more outlier beds than Unit 3 ($n = 18$), although the average recurrence, calculated from the EK14-1 age model (Section 4.2.4), is similar, 164 ± 99 and 231 ± 141 compared with 218 ± 187 years, respectively.

The frequency of outlier beds in core EK14-1 is lower than at other well-studied, higher-depositional rate sites, where they have multiple origins (Praet et al., 2017, 2020; Boes et al., 2018; Van Daele et al., 2020; Vandekerkhove et al., 2020; Schiefer et al., 2021). Core EK14-2, the closest long piston core to ours, which extends back through the CE, contains 44 outlier beds over the past 2.3 kyr compared with 14 in core EK14-1 over the same interval, consistent with thinning away from the inflow delta. We recognize, but do not include the 1964 CE earthquake deposit as an outlier bed, as an indistinct, 4-mm-thick, massive bed,

similar in depth and character to those found at nearby surface cores (Van Daele et al., 2020). The 1929 dam failure bed is present as a 2.0-cm-thick, sandy, grey bed, while the 1916 flood turbidite is a 1.5-cm-thick bed that subtly fines upward and is variegated. Other than these correlations with previously studied event layers, we do not assign our outlier beds to specific origins, although they likely formed from turbidity currents or avalanches. Additional outlier beds may be correlated with published records of event-based lake deposits (e.g., Praet et al., 2025); however, this will require additional work beyond the goals of this project.

4.2. Geochronology

4.2.1. Tephra

Sixteen tephra beds have been geochemically characterized by previous studies of Eklutna Lake cores, which extend back through the CE (Boes et al., 2018; Fortin et al., 2019; Praet et al., 2020; Thomas et al., 2021). Several have ages that are well constrained by varve chronology, while two older than the varve chronology have been correlated with tephra beds from outside the region (Boes et al., 2018; Bolton et al., 2020; Davies et al., 2024; Praet et al., 2025). Eight samples associated with prominent MS peaks were analyzed for this study. Seven contained abundant volcanic glass shards with one dominant geochemical population in each (Appendix A Table A1; Appendix A), confirming these MS spikes represent primary tephra deposits. Most of the tephra from core EK14-1 analyzed for this study were previously analyzed by Bolton et al. (2020); here, we present results from additional analyses from the same core that include two previously undescribed tephras (Section 4.2.2).

Four of these samples represent previously identified tephras from Eklutna Lake (EK-T5, EK-T10, EK-T12, and EK-T19) that have established ages, which were used to constrain the EK14-1 age model (Fig. 5; Table 1). Based on their glass composition, all are likely sourced from Redoubt Volcano (Bolton et al., 2020). Tephras EK-T5, EK-T10, and EK-T12 have assigned ages with 2σ error of 446 ± 24, 1287 ± 53, and 1723 ± 96 cal yr BP, respectively, based on varve counts and Bayesian modeling used to harmonize tephra ages among multiple cores within Eklutna Lake (Fortin et al., 2019; Praet et al., 2022, 2025). The age of EK-T12 is further supported in this study by a new correlation with tephras from Upper (UA 4428/CU1162) and Lower (UA4429/CU1149) Whitshed Lakes (Fig. 1B), which were analyzed along with the tephras from Eklutna Lake and date to 1719 ± 160 cal yr BP (Zander et al., 2018). The original EK-T12 samples exhibited greater scatter in their geochemistry, particularly in FeOt wt%. Re-analysis of EK-T12 for this study (UA 4246) using a higher-resolution sample (0.5 cm thickness instead of 1 cm) centered on the MS peak, eliminated the geochemical scatter observed in previous analyses, confirming the match with the Whitshed Lake tephras (Appendix A Fig. A1A and 1B). The oldest correlated tephra (EK-T19) is a 1-cm-thick white layer at a composite depth of 942 cm. This tephra is likely the regionally significant Oshetna-Redoubt ash, which has recently been suggested to geochemically correlate with a similar-aged tephra identified in the Greenland NGRIP ice core (sample GICC05 b1.95k, 6430 ± 38 cal yr BP; Davies et al., 2024).

Not re-analyzed here, but previously reported in core EK14-1 by Bolton et al. (2020), is the second-oldest tephra, EK-T18, which was identified as Hayes Tephra H2 (Wallace et al., 2014). Bolton et al. (2020) reported an age of 3713 ± 142 cal yr BP (IntCal13 chronology; Reimer et al., 2013) for Tephra H2 based on close-limiting radiocarbon ages derived from peat and wood above and below a tephra correlated with Tephra H2 from the Kenai Peninsula (Tephra T1; Combellick and Pinney, 1995). In addition to the 16 previously published tephras from Eklutna Lake, we present EK-T17, which was outside the existing age model when first reported by Bolton et al. (2020), and EK-T18b and EK-T20 for the first time here (Section 4.2.2).

4.2.2. Previously undated tephras

Three tephras from core EK14-1 did not have any age control prior to this study. Two of these are new tephras not previously reported from Eklutna Lake and with no firm regional correlations. Guided by past naming schemes used for Skilak and Eklutna Lakes, we refer to them here as EK-T18b (UA 4379/4465) and EK-T20 (UA 4466). EK-T17 was originally reported by Bolton et al. (2020) but, as noted above, was outside the existing age model for the core at the time. EK-T17 and T18b are geochemically similar tephras that are likely sourced from Redoubt Volcano (Table 1; Appendix A Fig. A1C and D; Bolton et al., 2020). Based on the EK14-1 age model (Section 4.2.4), their ages (± one half of the 95% confidence interval) are 2788 ± 325 and 6266 ± 252 cal yr BP, respectively (Table 1). The other new tephra, EK-T20, has glass major-element geochemistry that is consistent with other tephra sourced from Augustine Volcano and is dated here to 7032 ± 313 cal yr BP.

4.2.3. Radiocarbon

Twelve radiocarbon ages were obtained from EK14-1 based on terrestrial and aquatic macrofossils (Fig. 5; Table 2). The oldest macrofossil sample, a collection of plant remains, dates to 9647 ± 291 cal yr BP, taken from just 3 cm above the base of the composite core at 11.12 m (Fig. 5). The radiocarbon ages are largely in stratigraphic order, with one exception: a large partially burned wood fragment that was excluded from the age-depth model (Table 2).

Several lines of evidence indicate a hardwater effect (the assimilation of ^{14}C-depleted carbon from old carbon sources, resulting in anomalously old ^{14}C ages) on ^{14}C ages at Eklutna Lake. First, a *Gyraulus* sp. shell collected from the surface of the exposed lake margin yielded a ^{14}C age of 2557 ± 74 yr BP (Appendix A Table A2). Although the snail was not alive when collected, periostracum was present, and the shell is unlikely to have remained intact under shoreline lake ice. Thus, the aquatic snail was probably recently alive, and we suggest its unexpectedly low ^{14}C content is due to the presence of old dissolved inorganic carbon (DIC) in the lake. Next, at EK14-1, tephra EK-T12 (1723 ± 96 cal yr BP) is stratigraphically deeper (437.5 cm) yet younger than two nearby ^{14}C ages (2074 ± 210 and 2224 ± 181 cal yr BP at depths of 380.5 and 382.0 cm, respectively). One of the older ^{14}C samples contained fragments of *Drepanocladus*, an aquatic moss that likely assimilated old DIC (Table 2).

Furthermore, we suspect that deep groundwater flows into the lake, as evidenced by several spring-fed calcareous fens that are actively producing marl and tufa near the shoreline and within 1 km of EK14-1 (Fig. 2, Appendix A Table A3). Directly beneath one of the fens, a calcareous beach deposit was sampled from an outcrop (Appendix A Fig. A2) for paired biogenic carbonate and non-carbonate ^{14}C ages to test for a hardwater effect. Snail shell fragments dated to 10,001 ± 150 cal yr BP, whereas resting eggs and unidentified plants dated to 2151 ± 167 cal yr BP, demonstrating the presence of old DIC, although the extent to which the snails assimilated DIC from spring water versus lake water is not known. Another carbonate-rich layer from a calcareous bed within colluvium higher in the section showed a similar result. To our knowledge, this is the first report of these calcareous deposits. The inflow of carbonate-rich water is consistent with the circumneutral to slightly basic lake water chemistry (pH 7.4–8.6, averaging ~7.8 during the summer; Sauvageau and Schult, 2022, 2023).

4.2.4. Age model

Eight ^{14}C ages constrain the chronology of core EK14-1, together with three stratigraphic marker beds, five correlated tephra ages, and the age of the core top (2014 CE) (Fig. 5; Tables 1 and 2). Marker beds for the 1964 CE Alaskan earthquake, the 1929 CE dam collapse, and a 1916 CE flood turbidite (recently refined by Praet et al., 2025) were identified in core EK14-1 through stratigraphic correlation with previously dated lake sediment records (Boes et al., 2018; Vandekerkhove

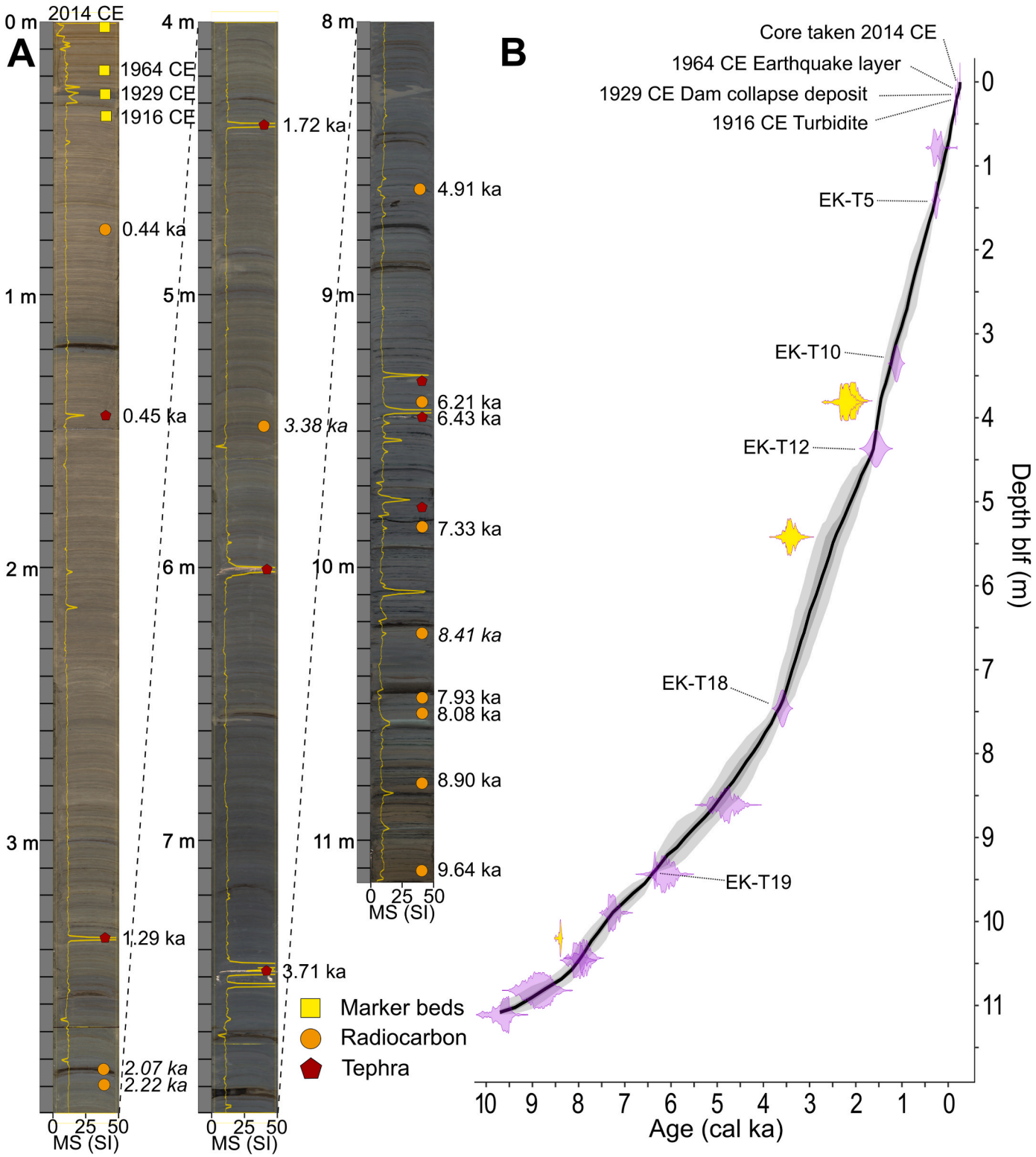


Fig. 5. Image and age-depth model for core EK14–1 from Eklutna Lake. (**A**) Composite image of sediment spliced from 11 core segments from three holes (Appendix A), divided into three panels and overlain by the magnetic susceptibility (MS) profile. Age constraints are shown based on our correlations with previously dated marker beds (Boes et al., 2018; Vandekerkhove et al., 2020), radiocarbon ages (cal ka), and correlated ages of tephras analyzed by single-grain microprobe analysis. (**B**) Age depth model created using Bacon (Blaauw and Christen, 2011) and plotted using geoChronR and lipdR (McKay and Emile-Geay, 2016; McKay et al., 2021). The grey ribbon represents the 95% confidence interval, the black line indicates the median age from 1000 ensembles, the purple probability distributions are the age-depth tie points and their associated error, and the yellow distributions are ^{14}C ages excluded from the model (Table 2).

et al., 2020). The age-depth relation (age model) for EK14-1 was developed using geoChronR (McKay et al., 2021), which employs rbacon (Blaauw and Christen, 2011) to generate a high-resolution (0.1 cm interval) age-depth relation in a Bayesian framework. Four ^{14}C dates were excluded from the age-depth model because they were inconsistent with the correlated tephra ages or were anomalously old relative to nearby ^{14}C ages (Fig. 5; Table 2). Tephras and outlier beds (Section 4.1.3) were treated as instantaneous deposits. To represent the observed changes in sedimentation (Table 3), accumulation-rate priors in the model were specified as 1.28, 1.0, and 0.5 mm yr^{-1} (7.83, 10, and 20 yr cm^{-1}) for Unit 1, Unit 2, and Unit 3 (Section 4.1.2), respectively. The average modeled 95% confidence interval, evaluated at 1 cm intervals, is ±217 years.

4.3. Biological, physical, and chemical properties

4.3.1. Organic productivity (OM, BSi, and RABD$_{660;670}$)

All three organic productivity indicators – BSi, OM, and RABD$_{660;670}$ – are characterized by low concentration. Their downcore trends are generally similar, but with important differences (Fig. 3). All three are higher over the first half of the record (Units 1 and 2), except BSi, which shifts to low values in subunit 2b. This divergence results in a non-significant ($p > 0.05$) correlation between the BSi time series and both OM and RABD$_{660;670}$ (Table 4). In contrast, OM and RABD$_{660;670}$ are significantly correlated overall ($p = 0.009$), but diverge in the lower half of Unit 3, where OM decreases while RABD$_{660;\ 670}$ increases. In the top ~40 cm of the core, RABD$_{660;670}$ and OM both increase sharply. RABD$_{660;670}$ values generally vary between 1.00 and 1.02, indicating extremely chloropigment-poor sediment; nevertheless, the strong correlation between RABD$_{660;670}$ and OM suggests that even these small changes in RABD$_{660;670}$ capture meaningful downcore variability in sediment composition.

4.3.2. Sedimentation rate

Sedimentation rates were computed based on the median of 1000 age ensembles at each centimeter depth. These rates were then binned into 500-year intervals to reduce overinterpretation of rate shifts, which often coincide with the depths of each date in the age model. The sedimentation rate increases upward from an average of 0.33 mm yr^{-1} in Unit 1 to 2.17 mm yr^{-1} in Unit 3 (Table 3). Sedimentation rates reach their highest 500-year average (0.37 cm yr^{-1}) in the last half millennium, despite no noticeable decrease in WBD. Sedimentation rate is inversely related to all three productivity indicators (Fig. 6), which is consistent with dilution of organic constituents by mineral matter and the concurrent reduction in aquatic productivity in response to increased turbidity. The timing of the sedimentation rate uptick around 3.5 ka coincides more closely with OM and RABD$_{660;670}$ than with BSi.

4.3.3. Particle size distribution

The sediment in EK14-1 is dominated by silty clay, with an average median grain size (D50) of 3.7 μm (Fig. 3). EMM decomposed the particle size distributions into four grain size end members (Fig. 7). EM1 consists of clay (<2 μm) and very fine silt (2–7.8 μm) and accounts for 46.1% of the variance. EM2 comprises fine and medium silt (7.8–31 μm; 36.3%), while EM3 represents a bimodal mixture of clay (~0.5 μm) and silt (≥4.0 μm; 13.3% variance). EM4 corresponds to a coarse silt and sand fraction (≥31.0 μm) and explains 4.2% of the variance. The fine–medium silt component (EM2) dominates Units 1 and subunit 2a. EM1 remains low until Subunit 2a, when it becomes mixed with EM2 and EM3 through the remainder of Unit 2, eventually becoming the most dominant (Fig. 7D).

4.3.4. Geochemistry

Downcore XRF data were used to quantify relative differences in the composition (CLR) of elements with high counts in core EK14-1, including Si, K, Fe, and Ca (Table 3, Fig. 4). On average, Unit 1 is depleted in Si and enriched in Fe, Unit 2 is enriched in K and Ti, and Unit 3 in Ca. The time series of Ca abundance correlates with several clastic and productivity indicators (Table 4), but with some notable differences. In light of the evidence for Ca-rich spring discharge near the lake (Section 4.2.3), we conducted an extended investigation into the source of Ca in the lake sediment to help explain these differences. The findings, which are detailed in Appendix A (Section A3), suggest a groundwater source, although other sources likely contribute Ca as well. Changes in the Ca and other elemental abundances of the sediment are only marginally related to changes in particle size (correlations not reported

Table 4
Correlation matrices for biological and physical properties of core EK14-1. (**A**) Pearson's correlation coefficient (*r*) and (**B**) *p*-values from isospectral significance testing with *p*-values <0.05 in bold.

	BSi	OM	RABD$_{660;670}$	Sed. rate	WBD	Si/Al	Ca (CLR)	D50	EM1	EM2	EM3
A. *r*-values											
BSi	1										
OM	0.492	1									
RABD$_{660;670}$	0.502	0.511	1								
Sed. rate	−0.579	−0.571	−0.619	1							
WBD	−0.818	−0.492	−0.355	0.505	1						
Si/Al	0.126	−0.454	−0.232	0.223	−0.070	1					
Ca (CLR)	−0.504	−0.788	−0.528	0.639	0.552	0.494	1				
D50	0.424	0.055	0.419	−0.385	−0.430	0.128	−0.155	1			
EM1	0.536	−0.294	0.479	0.558	0.732	−0.239	0.362	−0.721	1		
EM2	0.533	0.056	0.256	−0.293	−0.531	0.402	−0.103	0.604	−0.865	1	
EM3	0.552	0.503	0.556	−0.487	−0.617	−0.219	−0.590	0.482	−0.621	0.167	1
B. *p*-values											
BSi	1										
OM	0.292	1									
RABD$_{660;670}$	0.081	**0.009**	1								
Sed. rate	**0.025**	**0.016**	**0.001**	1							
WBD	**0.000**	0.515	0.488	0.193	1						
Si/Al	0.828	0.378	0.430	0.697	0.927	1					
Ca (CLR)	0.440	**0.014**	**0.002**	**0.002**	0.522	0.430	1				
D50	0.123	0.914	0.085	0.097	0.178	0.742	0.787	1			
EM1	**0.016**	0.634	0.126	0.087	**0.005**	0.624	0.598	**0.000**	1		
EM2	**0.027**	0.902	0.329	0.199	**0.004**	**0.040**	0.833	**0.003**	**0.000**	1	
EM3	0.114	0.278	**0.036**	0.075	0.126	0.680	0.263	0.059	**0.045**	0.553	1

in Table 4, other than for Ca and Si/Al). Instead, elemental differences among units might be related to changes in the relative proportion of sediment derived from the most heavily glaciated tributaries, even though the bedrock of the catchment is a heterogeneous meta-sedimentary and meta-volcanic mixture (Winkler, 1992).

We found that inflow sediments from the highly glaciated portions of the catchment (East Fork and West Fork) showed subtle differences in their geochemical composition compared to those from non-glaciated

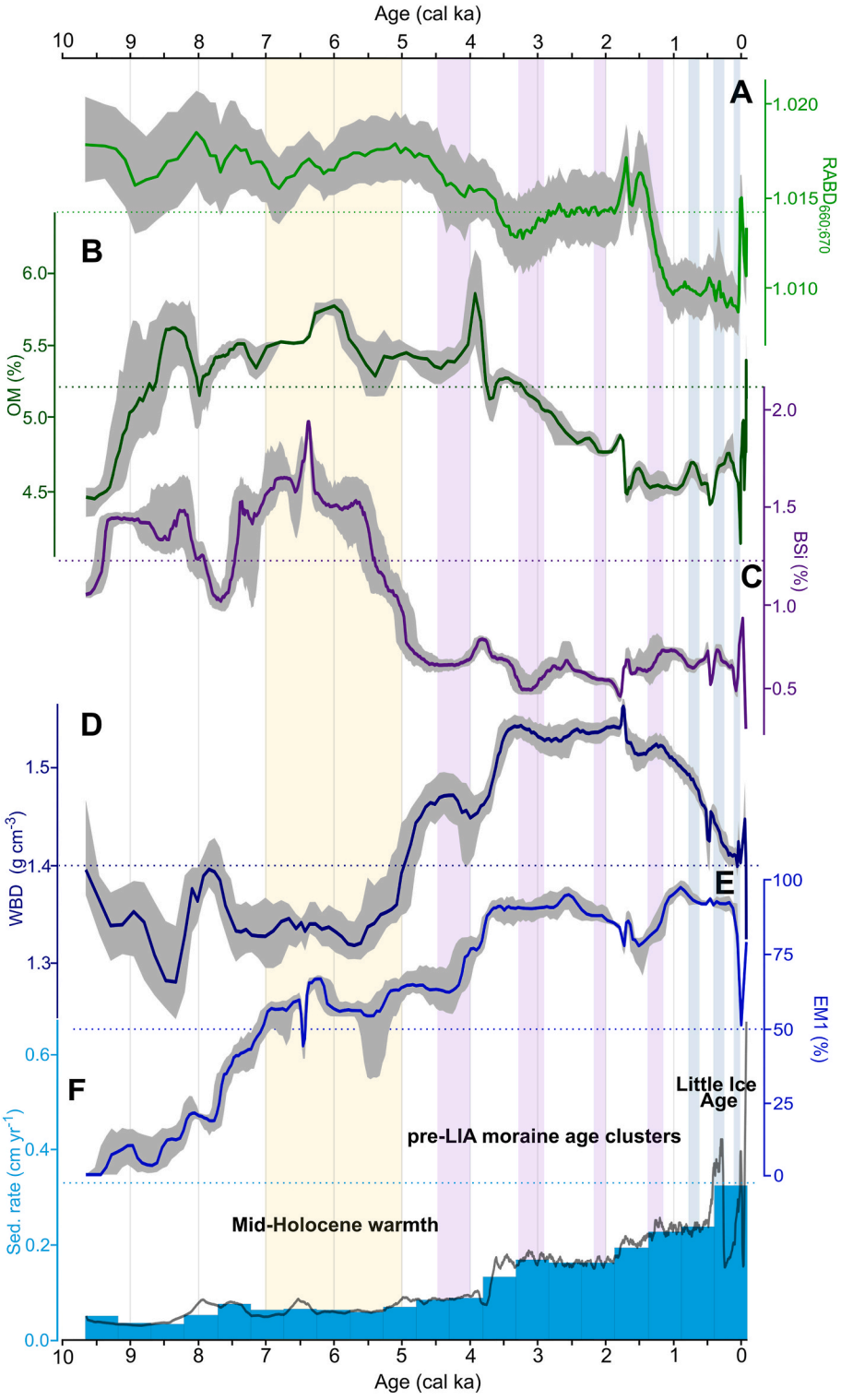


Fig. 6. Core EK14–1 selected biological and physical properties plotted by age. Bold lines are median ensemble values shown with the 0.25–0.75 confidence interval (grey shaded ribbons). Yellow vertical bar marks the mid-Holocene warm interval (Kaufman et al., 2016); light purple bars mark Alaska moraine age clusters (Solomina et al., 2015); sky blue bars show the three-part Little Ice Age (Barclay et al., 2009). (**A**) Total chlorin abundance inferred from hyperspectral measurements of $RAD_{660;670}$. (**B**) Organic matter (OM) abundance measured by loss on ignition. (**C**) Biogenic silica (BSi) abundance. (**D**) Wet bulk density (WBD) measured via gamma ray attenuation. (**E**) End member 1 (EM1) from end member modeling of grain size distribution (Fig. 7). (**F**) Sedimentation rate shown as 500-year bins and a 10-point (10 cm) running average (grey line).

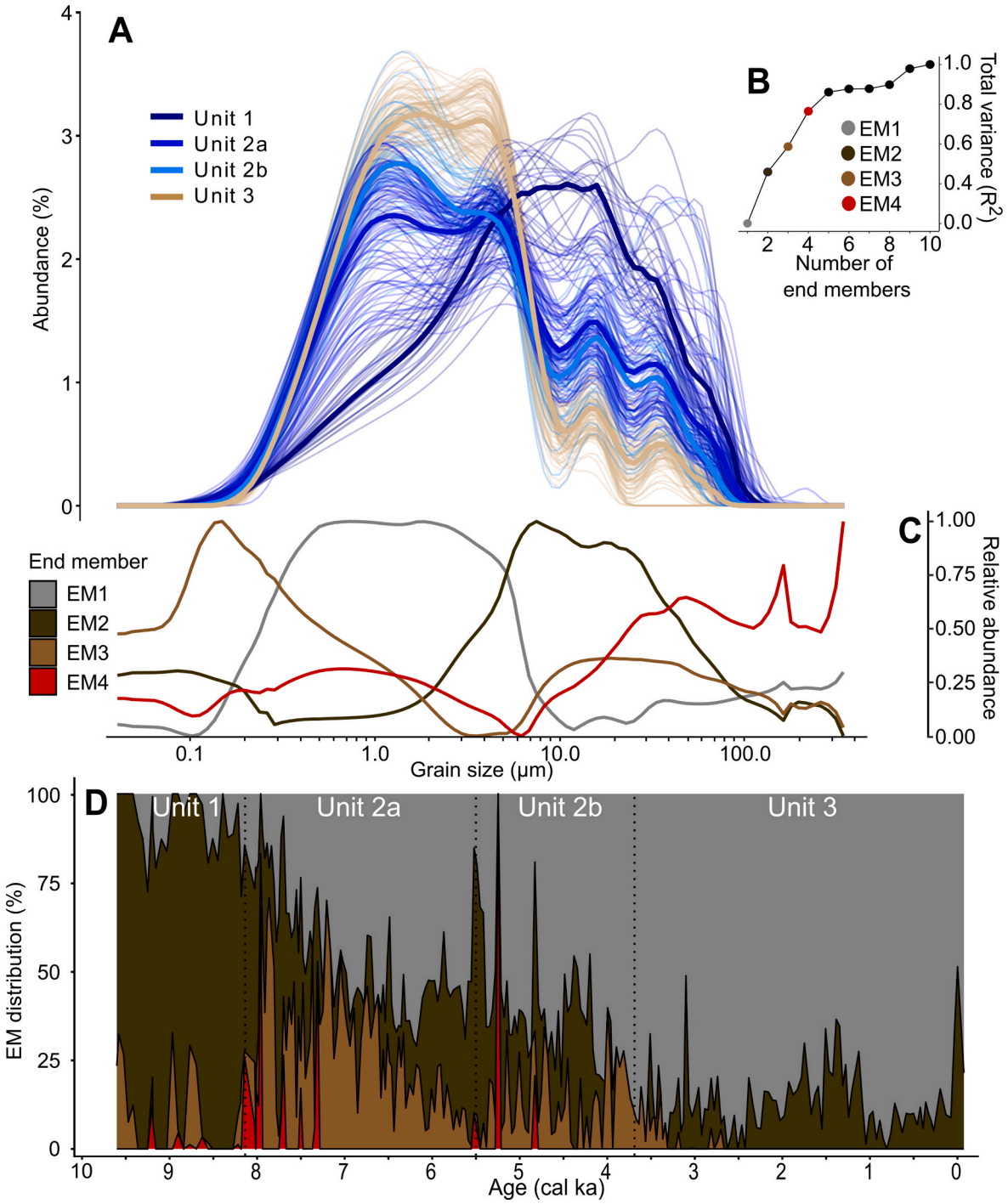


Fig. 7. Particle size end member (EM) modeling output for core EK14–1. (**A**) Particle size distributions of individual samples from each stratigraphic unit (color coded), with median distribution per unit shown in bold. (**B**) Goodness-of-fit plot showing diminishing benefit beyond the first four end members. (**C**) Relative abundance of grain sizes for each EM. (**D**) Stacked area plot showing the contribution of each EM by age and color-coded as in panels B and C. Unit boundaries are delineated with dotted vertical lines. Note that panels A and C share a common x-axis.

streams. The XRF counts are high for Si and low for K in the rock-flour-rich outwash streams, and we use these elements ratioed against Al for mineralogical inferences. Namely, the relatively high Si/Al ratio indicates that the rock flour is depleted in clay minerals compared with stream sediment in the non-glaciated tributaries, which are mainly underlain by Valdez Group rocks dominated by siltstones and mudstones (flysch) (Winkler, 1992). Likewise, the low K/Al ratio of the rock flour is consistent with the high abundance of K-feldspars in McHugh Complex rocks (Clark, 1973). As expected, Ca (and $CaCO_3$) is orders of magnitude higher in sediment from the calcareous fens than in other inflows (Appendix A Section A3.3). The loess elemental composition is generally intermediate between the East Fork and West Fork and other inflows, with no diagnostic enrichment of particular major elements.

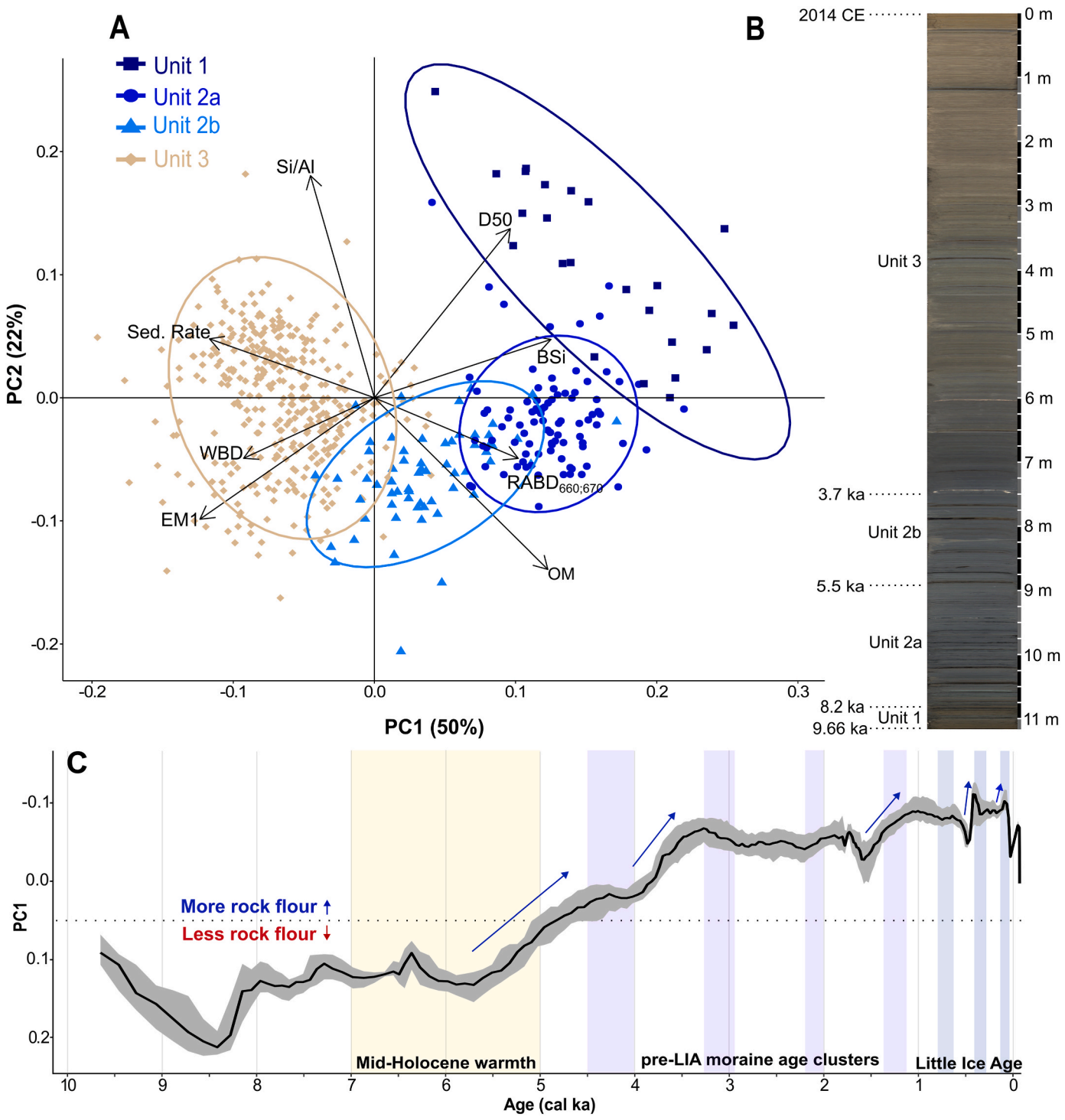


Fig. 8. Principal component analysis (PCA) of multiple biological and physical properties from core EK14–1. (**A**) Ordination plot of individual samples ($n = 542$), 95% prediction ellipses, and loading vectors subdivided by stratigraphic units, shown in (**B**) the composite core image. (**C**) Time series of PC1with 0.25–0.75 confidence intervals (grey ribbon). More negative values represent increased rock flour deposition at the core site. See Fig. 6 for description of vertical bars and text for discussion of blue arrows.

5. Discussion

5.1. What is the best indicator of rock flour in Eklutna Lake?

Proglacial lake sediments record glacier fluctuations through variations in the delivery of glacially derived rock flour. Shifts in minerogenic content, density, particle size, magnetic properties, aquatic and terrestrial organic matter, elemental geochemistry, and sedimentation rate are widely used to infer glacier fluctuations within the lake catchment (e.g., Karlén, 1981; Lemmen et al., 1988; Desloges, 1994; Noon et al., 2001; Levy et al., 2004; Rosenbaum and Reynolds, 2004; Stansell et al., 2013). Because these properties are all indicators of changing rock flour abundance, they should correlate strongly. At Eklutna Lake, they mostly do; however, we also find differences in trends and timing of changes that complicate the interpretation of rock flour abundance, obscuring a direct signal of glacier change. In addition, many studies that

successfully use downstream lake sediment to reconstruct glacier fluctuations feature catchments where high glaciated tributaries are underlain by igneous rocks (e.g., granitic stocks) while the low unglaciated tributaries are in sedimentary rocks (e.g., Waskey Lake; Levy et al., 2004), thereby amplifying the rock flour signature due to lithological differences between glaciated and non-glaciated tributaries. In contrast, such geochemical differences are only weakly expressed within the Eklutna Lake catchment (Appendix A Table A3), most likely because the bedrock is largely composed of similar mineral assemblages (Clark, 1973; Winkler, 1992). Furthermore, at Eklutna Lake, MS values are dominantly influenced by episodic tephra deposition rather than rock flour, and other magnetic properties have not been investigated. Likewise, the mineral content, which might provide evidence for sediment provenance, has not been studied on the EK14-1 core.

Bulk density, sedimentation rate, and changes in particle size are among the most widely used indicators of rock flour deposition in proglacial lakes (Leonard, 1997; Leonard and Reasoner, 1999; Matthews et al., 2000; Dahl et al., 2003; Bakke et al., 2005a, 2005b). At Eklutna Lake, WBD and sedimentation rate are not significantly correlated (Table 4); however, the datasets exhibit similar trends throughout the record (Fig. 6). Further, particle size in proglacial lakes reflects a combination of sediment source and supply, inflow proximity and discharge, the intensity of underflows, and lake level, but only some of these variables are glacier-size dependent (Smith and Ashley, 1985; Desloges and Gilbert, 1994; Schiefer and Gilbert, 2008). To separate these influences, EMM can be applied to the grain size data to help isolate the glacially derived end member (Lemot et al., 2024; Auer et al., 2025). We interpret EM1, which is dominated by clay and very fine silt, to mainly represent rock flour in core EK14-1. EM1 is weakly correlated with sedimentation rate and is significantly correlated with WBD (Table 4), indicating that elevated clastic input and higher bulk density coincide with increased concentrations of very fine silt and clay particles. EM1 begins to increase ~8 ka, most likely attributed to a rise in lake level (Section 5.3.1) and becomes the most prominent end member (>~50%) in the core by ~7 ka (Fig. 6E), several millennia earlier than increases in WBD and sedimentation rate. EM1 then dominates (>~80%) beginning around 3.7 ka. We interpret the rise in EM1 ~7 ka as the initial expansion of glaciers in the catchment, but cannot rule out the possibility that non-glacial processes, which act on the same bedrock type as the glaciers, also contribute to EM1.

Our three productivity indicators (OM, $RABD_{660;670}$, BSi) are generally highest during the interval of 7.0–5.0 ka (Fig. 6); however, BSi exhibits a significant decline at 5.5 ka, whereas OM and $RABD_{660;670}$ decrease more gradually, with OM remaining relatively high until 3.5 ka (Fig. 6). Similar to BSi, WBD shows a notable transition to higher values around 5.5 ka and the two are inversely related ($r = -0.818$, $p < 0.001$). The strong correlation suggests that WBD is associated with BSi content, which influences sediment porosity. Additionally, $RABD_{660;670}$ initially declines around 4.5 ka but is not significantly diminished until 1.5 ka, a trend not seen in OM or BSi. OM and $RABD_{660;670}$ are indicators of environmental productivity (both autochthonous and allochthonous), while BSi reflects autochthonous productivity only. Because rock flour suspended in glacier-fed lakes accounts for roughly two-thirds of light attenuation (Rose et al., 2014), fluctuations in turbidity directly influence how much sunlight reaches the photic zone, thereby affecting photosynthetic productivity and BSi production. This may explain why transitions in BSi decouple from OM and $RABD_{660;670}$, which can be influenced by both aquatic and terrestrial sources. In addition to changes in lake turbidity, seasonal and long-term ice cover, which is controlled by local air temperature, have been shown to significantly influence BSi production in Arctic and proglacial lakes (Douglas and Smol, 1999; McKay et al., 2008), also potentially decoupling terrestrial and aquatic productivity.

OM is commonly used as a proxy for glacier variability in proglacial lakes (Karlén, 1976; Nesje et al., 2000; Noon et al., 2001; McKay and Kaufman, 2009). Bulk sediment density should inversely reflect the abundance of OM in proglacial lake sediment, as organic matter has a lower density than minerals and it also increases sediment porosity. In EK14-1, OM and WBD are not correlated ($p = 0.515$), and WBD declines through the last ~1.1 ka, when all productivity indicators are, on average, at their lowest in the record. These somewhat contrary shifts suggest that clastic sediment indicators and OM respond differently to environmental forcings, potentially influenced by catchment-specific processes.

5.1.1. Using multivariate analysis to find a rock flour signature

Principal Component Analysis (PCA) was used to identify the main patterns of covariation among multiple biological, physical, and chemical properties. By reducing the dataset to several orthogonal components that capture the most variance, PCA isolates shared signals, such as those related to rock flour abundance, from noise or property-specific variability. This enables us to quantify and visualize the primary variability in our entire dataset, which we interpret as rock flour input over time. PCA has previously been used in a similar way as a holistic approach to quantify and isolate specific patterns in ice-distal proglacial lakes to reconstruct glacier changes through time (Vasskog et al., 2012; Bakke et al., 2013; Røthe et al., 2015; Wittmeier et al., 2015; Larocca et al., 2020).

PCA was applied to the combined geochemical, sedimentological, and EMM datasets (Fig. 8). Because the multiple variables that quantify particle size are largely intercorrelated, we included only two, EM1 and D50, which we interpret as the strongest and most independent indicators of rock flour. For elemental composition, we included Si/Al, the ratio that best captures the contrast between glaciated and non-glaciated catchment sources as determined by our stream sediment samples (Appendix A Table A3). PC1 explains 50% of the variance, and PC2 explains 22% (Fig. 8A). The loading vectors highlight the distinguishing features of each unit as described previously (Table 3). Namely, Unit 1 is distinguished largely by its coarse grain size (D50); Unit 2 by its high productivity values (OM, $RABD_{660;670}$, BSi); and Unit 3 by its fine particle sizes that dominate EM1, and its higher WBD, Si/Al, and sedimentation rate.

5.2. Relation between rock flour abundance and glacier extent

5.2.1. Sediment production, glacier size, and complicating factors

On centennial to millennial timescales, the volume of rock flour generated by a glacier and delivered to a downstream lake is largely determined by the glacier's size. Hallet et al. (1996) compiled sediment yield data from glacierized basins worldwide and demonstrated that sediment yield scales positively with glacier coverage. The mechanistic basis is straightforward: a larger glacier-covered area is associated with more basal contact between sliding ice and bedrock, sustaining higher rates of abrasion and quarrying that generate rock flour, which is then entrained by subglacial streams and transported by proglacial meltwater to lake sinks. In southern Alaskan catchments, where abundant winter precipitation drives high mass turnover and rapid ice motion, the connection between glacier extent and downstream sediment flux is especially pronounced (Lawson, 1993; Hallet et al., 1996).

However, several factors modulate or complicate the first-order relationship between glacier size and rock flour production. A global synthesis of glacial erosion rates found that, while glacier sliding velocity is an important control on abrasion and quarrying, its influence is context-dependent and interacts with glacier geometry, climate, and substrate properties (Norris et al., 2025). For example, precipitation amount influences erosion in part by increasing subglacial meltwater flux, which can flush protective layers of till from the glacier bed to expose fresh bedrock to abrasion and quarrying (Alley et al., 2019; Delaney and Adhikari, 2020). Changes in subglacial hydrology also influence how efficiently rock flour is evacuated to the terminus; channelized drainage exports fine sediment effectively, whereas distributed systems promote storage that can decouple production from delivery

(Fenn, 1987; Werder et al., 2013). Short-term pulses of sediment delivery during accelerated glacier melt reflect transient increases in meltwater flux, sediment evacuation, and transport efficiency rather than sustained changes in erosive capacity (Alley et al., 2019). Paraglacial reworking can cause sediment yields to reflect redistribution of legacy glacial deposits rather than contemporaneous erosion, though this effect is most pronounced immediately following rapid deglaciation and declines as legacy stores are exhausted (Church and Ryder, 1972; Leonard, 1997). Despite these complications, we interpret the Holocene record of rock flour in Eklutna Lake primarily as a proxy for glacier extent and proximity to the lake. Glacier size and length are themselves among the strongest predictors of erosion for land-terminating glaciers (Norris et al., 2025), and the other modulating factors either co-vary with the climatic forcing that drives glacier expansion, which reinforces the glacier-size signal, or operate on timescales shorter than the centennial resolution of this study.

5.2.2. Correspondence with Alaska-wide glacier history

Using rock flour as a proxy for glacier extent is further supported by the correspondence between rock flour abundance at Eklutna Lake and the independently documented history of glacier fluctuations across Alaska, reconstructed from dated glacial geomorphic features, principally moraines. Low rock flour abundance prior to ~5.5 ka reflects limited glacier extent, consistent with warm summer conditions (Kaufman et al., 2016) and the widespread retreat and disappearance of glaciers and ice caps across the Arctic between ~8.0 and 6.5 ka (Larocca and Axford, 2022). Rock flour abundance increases roughly in synchrony with the onset of Neoglacial cooling between 6 and 5 ka in Alaska and the Yukon (McKay et al., 2018), consistent with evidence for initial glacier advance in the region at this time (Section 5.3.3).

Reviews of Alaska Holocene glacier history based on moraine ages generally identify four Neoglacial age clusters prior to the LIA (Barclay et al., 2009; Solomina et al., 2015; Kaufman et al., 2016, Fig. 8C), and the expected temporal relationship between glacier dynamics and moraine formation provides a framework for comparison. As glaciers advance, erosion and rock flour production increase; moraines are deposited at or near the limits of advance, recording the culmination of expansion rather than its onset. We therefore expect rock flour abundance to rise during the advance phase that precedes moraine formation, and for moraine ages to coincide with intervals of elevated but stabilizing rock flour accumulation. We find shifts in rock flour abundance at Eklutna Lake that largely correspond with the regional moraine-age clusters from around Alaska (Fig. 9). Given the multi-century uncertainties inherent in both the moraine-age clusters and the Eklutna Lake rock flour time series, the expected sequence of rising rock flour preceding moraine formation appears to hold for three of the four pre-LIA clusters: 4.5–4.0, 3.3–2.9, and to some extent 1.4–1.1 ka. The rise in rock flour associated with the 2.2–2.0 ka cluster is more subdued than the others, possibly reflecting more limited glacier expansion or local catchment effects that attenuate the signal.

Generally glaciers across Alaska reached their maximum Holocene extent during the LIA (Barclay et al., 2009; Wiles et al., 2008; Solomina et al., 2015, 2016), and the Eklutna Lake record shows its maximum rock flour abundance at precisely that time. This correspondence constitutes strong evidence that ice extent is the dominant control on the sediment signal. PC1-inferred rock flour abundance reaches its second-highest value around 1550 CE and sustains a prolonged high before reaching the record's maximum near 1880 CE, broadly coinciding with the two most prominent LIA glacial phases identified across Alaska (1540s–1710s and 1810s–1880s CE; Wiles et al., 2008; Barclay et al., 2009; Solomina et al., 2016). These two peaks centered at 1547 ± 89 CE, and 1882 ± 36 CE fall within recognized LIA phases and may correspond to the prominent end moraines fronting Eklutna Glacier as mapped by Brabets (1993) and clearly expressed in high-resolution digital elevation models (DEMs), although the absence of age control on these features precludes a definitive assignment. Taken together, the coherence between the Eklutna Lake rock flour record and the Alaska-wide pattern of moraine formation across multiple Neoglacial advances, culminating in the LIA maximum and decreasing with 20th century retreat, strongly supports the interpretation that rock flour abundance at this site tracks glacier extent through the Holocene.

5.3. Holocene paleoglacier and lake-level fluctuations

5.3.1. Low lake level 9.6–8.2 ka

Grain size in lacustrine environments is strongly influenced by wave energy and proximity to the shoreline, with coarser grains deposited under higher-energy nearshore conditions and finer sediments accumulating in deeper areas, such that particle size can be used to infer past lake-level fluctuations (Håkanson and Jansson, 1983; Xiao et al., 2009). Because EK14-1 is located in only 21 m of water (during coring in spring, 2014), away from steep valley walls and not in the depocenter where coarser particles can accumulate through turbidites and hyperpycnal flows, it should be sensitive to past lake-level fluctuations. Unit 1 is notably coarser than the overlying units (Table 3) with distinct 1- to 3-cm-thick brown beds not observed elsewhere in the core. Grain size EM2 dominates Unit 1 (average 83.4%), suggesting a distinct sediment source, as indicated by its high Fe and low Si relative abundance, and/or a high-energy depositional setting. In addition, nearshore conditions are associated with low sedimentation rates, as sediment is focused toward the depocenter. At EK14-1, the average sedimentation rate is lowest in Unit 1 (Table 3). Furthermore, in the seismic stratigraphy, core EK14-1 penetrates ~0.6 m of the high-amplitude reflections of Seismic Unit 1 and likely corresponds to Unit 1 in core EK14-1. These more chaotic beds with high-amplitude reflectors suggest a more nearshore and shallower environment compared to the stratified sediments of Seismic Unit 2 above. We interpret the high-amplitude and less-stratified seismic facies in Seismic Unit 1, the low sedimentation rate, and the high abundance of coarse grains (EM2) in Unit 1 as reduced lake depth during the early Holocene.

The sedimentary evidence aligns with other evidence for lower lake levels from the region. An earlier review across Alaska and Yukon showed that lake levels were generally well below their late Holocene levels prior to 9 ka (Kaufman et al., 2016). More recent studies from several lakes in southern Alaska reinforce the finding of low lake levels until around 8 ka (Broadman et al., 2020a; Berg et al., 2022; Wobleski et al., 2023). During this period, the Kenai Peninsula was relatively warm and dry (Anderson et al., 2006, 2019; Jones et al., 2009; Wobleski et al., 2023). At Hundred Mile Lake, a pronounced decrease in $\delta^{18}O$ between 10.5 and 8.0 ka has been interpreted as evidence for a major shift in atmospheric circulation patterns (Yu et al., 2008). While the dominant moisture source remained the Gulf of Alaska via the westerlies, the depleted $\delta^{18}O$ values indicate an increase in dry easterlies, either shifting the trajectories of water vapor coming from the Pacific Ocean or forcing the moist air to condense at higher altitudes (Yu et al., 2008). These regional records indicate substantial changes in atmospheric circulation, temperature, and aridity during the early Holocene, factors that likely influenced the hydrologic balance at Eklutna Lake.

The decline in EM2 dominance after ~8.2 ka indicate rising lake levels, consistent with the timing seen at multiple lakes in southern Alaska (Anderson et al., 2006; Broadman et al., 2020a; Berg et al., 2022; Wobleski et al., 2023) and more broadly across eastern Beringia (Kaufman et al., 2016). The contact between Unit 1 and Unit 2 is marked by an outlier bed and seems to be represented as an abrupt change in the sub-bottom profile (Fig. 2E). Although the shift roughly coincides with cold conditions associated with the 8.2 ka event known from the North Atlantic region, there is no evidence in EK14-1 for a short-lived excursion with a return to pre-8.2 ka conditions.

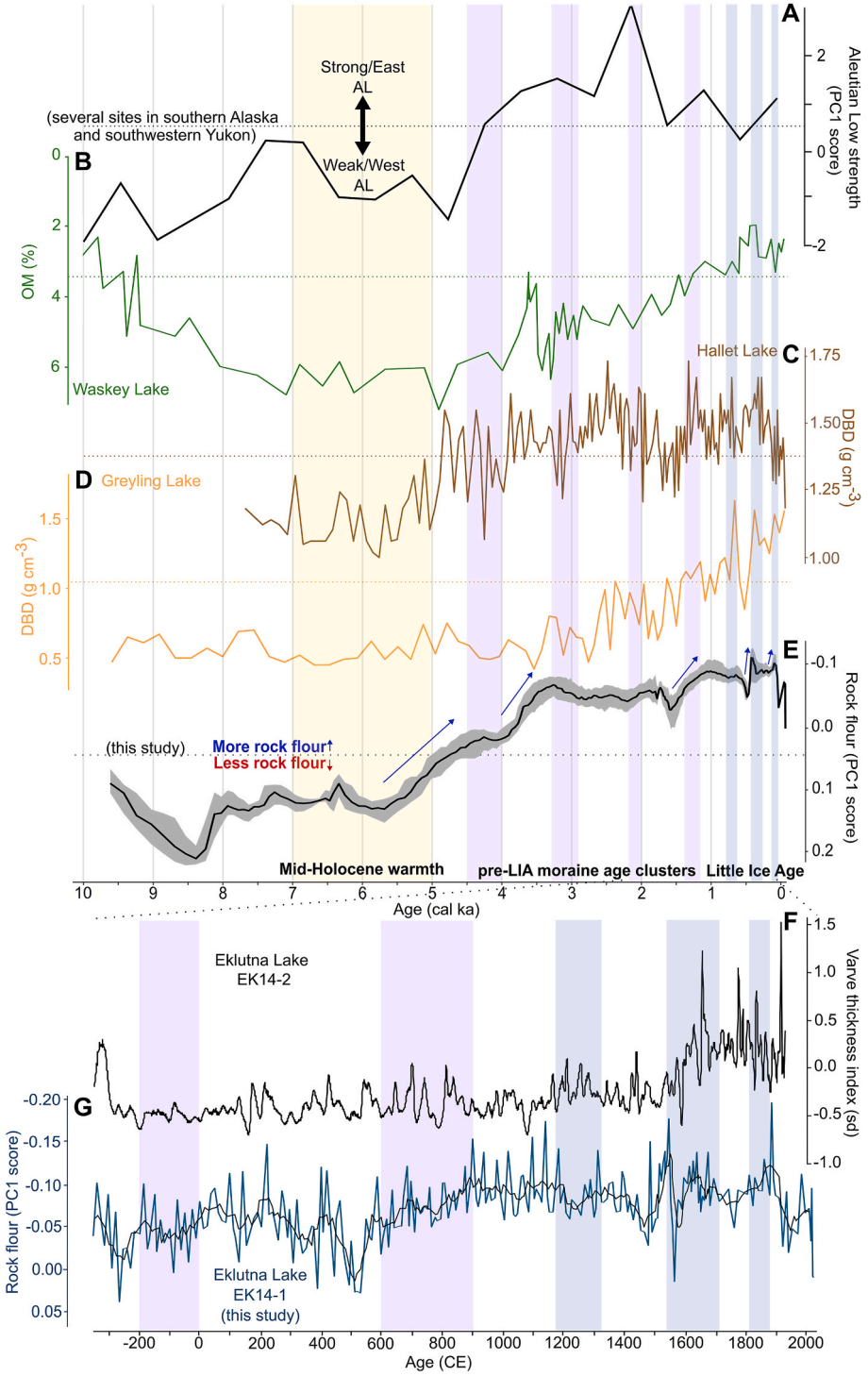


Fig. 9. Selected records of inferred Holocene glacier extent from southern Alaska and Aleutian Low strength. (**A**) PC1 time series of Aleutian Low variability from southern Alaska and southwestern Yukon (Broadman et al., 2020b). (**B**) Time series of organic matter (OM) abundance from Waskey Lake, Ahklun Mountains, southwestern Alaska (Levy et al., 2004) plotted here on an updated age-depth model using Bacon (Blaauw and Christen, 2011) and geoChronR and lipdR (McKay and Emile-Geay, 2016; McKay et al., 2021). (**C, D**) Dry bulk density (DBD) time series from proglacial Hallet and Greyling Lakes, Chugach Mountains, south-central Alaska (McKay and Kaufman, 2009). (**E**) PC1 from core EK14-1, Eklutna Lake. (**F, G**) Enlargement of the Common Era (CE), including (**F**) varve thickness index for core EK14-2, Eklutna Lake (Thomas et al., 2021), compared to (**G**) PC1 from core EK14-1 Eklutna Lake. The black line is a 5-point running average. See Fig. 6 for description of vertical bars and text for discussion of blue arrows.

5.3.2. Retracted glaciers until 5.5 ka

Evidence for early Holocene glacier extent in Alaska remains sparse, with few available continuous records of rock flour deposition from ice-distal proglacial lakes like Eklutna Lake. Reviews of Holocene Alaskan valley glaciers conclude that many glaciers retracted into their cirques prior to the start of the Holocene (Barclay et al., 2009; Solomina et al., 2015; Kaufman et al., 2016), and there is limited evidence of glaciers advancing during the late glacial or early Holocene. High-elevation areas like Mt. Hunter in the central Alaska Range had glacier-ice cover during the early Holocene (Fig. 1B; Fang et al., 2023). At Goat Lake

(Kenai Peninsula), the North Goat Glacier remained advanced above a topographic divide, depositing glaciolacustrine sediments until ~9.5 ka (Fig. 1B; Daigle and Kaufman, 2009). In the Ahklun Mountains, Waskey Lake records continuous rock flour input until 9.1 ka (Fig. 1A; Levy et al., 2004). Only one site in Alaska shows clear evidence for an early Holocene advance. At Emerald Lake (Fig. 1B; Kenai Peninsula), the Grewingk Glacier retreated from the lake catchment by 11.4 ka. It then re-entered the lake catchment at 10.7 ka, where it remained until retreating again at 9.8 ka (LaBrecque and Kaufman, 2016). We conclude that the base of core EK14-1 at 9.6 ka is too young to record any early Holocene readvance that might have occurred in the region.

PC1 values peak around 8.5 ka, indicating the lowest rock flour abundance in the sequence. While this might represent the Holocene minimum in rock flour abundance, the rock flour signal could also be confounded by different sedimentation processes associated with this low-lake interval. PC1 values remain high until around 5.5 ka, indicating minimal glacier influence at Eklutna Lake up until this time, and no moraines in the catchment are known to record glacier positions from this interval. This is consistent with regional evidence for reduced glacier extent under relatively warm mid-Holocene conditions (Kaufman et al., 2016), including at Hallet and Greyling Lakes (10–6 ka; McKay and Kaufman, 2009) and Waskey Lake (9.1–3.1 ka; Levy et al., 2004), where glaciers were interpreted as absent or substantially diminished (Fig. 9B, C, D). Proglacial threshold lakes on the Kenai Peninsula also align with the EK14-1 record, showing that glaciers during the mid-Holocene were smaller than during the LIA (Daigle and Kaufman, 2009; LaBrecque and Kaufman, 2016). Overall, PC1 values during the mid-Holocene (Fig. 8C) suggest that glaciers were less extensive than they are now. However, the relation between PC1 values, rock flour abundance, and glacier extent may not be entirely linear.

5.3.3. Early Neoglacial advances

PC1 at Eklutna Lake indicates increasing rock flour deposition from 5.5 to 3.5 ka, by which time glaciers likely neared their modern limits, as PC1 values at this time are comparable to those of present-day. At Hallet Lake, DBD similarly increased between 5.5 and 4.0 ka, indicating advancing glaciers (McKay and Kaufman, 2009). Additionally, the Mt. Hunter ice core captured increased snow accumulation between 5 and 3 ka (Fang et al., 2023). More broadly, proxy records from across Alaska and the Yukon show a peak in the onset of Neoglacial cooling around 6 ka (McKay et al., 2018). PC1 values reach near LIA levels around 3.3 ka, aligning with regional reconstructions that show many glaciers during the early Neoglacial period (4.5–3.0 ka) advanced to positions comparable to their LIA extents (Kaufman et al., 2016).

The largest transition in PC1, which is centered around 4 ka, coincides with a major shift toward a stronger and more easterly Aleutian Low, as documented across Alaska (Fig. 9A) (Broadman et al., 2020b, and references therein). Changes in the Aleutian Low, a semi-permanent low-pressure system over the North Pacific (Overland et al., 1999), has exerted a primary control on winter precipitation delivery to Alaska during the Holocene (e.g., Heusser et al., 1985). Holocene reconstructions from peat, ice-core, and lake-sediment records indicate a weaker, more westerly Aleutian Low from 10 to 4 ka, and a stronger, more easterly Aleutian Low from ~4 ka to the present (Fig. 9A; Broadman et al., 2020b). The onset of the latter regime aligns with increasing rock flour delivery at Eklutna Lake. Cooler temperatures and increased winter-time precipitation likely promoted sustained glacier growth after ~4 ka and helped maintain advanced glacier positions through the remainder of the Neoglacial.

5.3.4. Common Era and comparison to core EK14-2

During the CE, PC1 from EK14-1 reflects sustained rock flour input that intensifies through the first millennium and again during the LIA, culminating in the highest rock flour abundance of the entire Holocene (Fig. 9E–G). Following 1900 CE, PC1-inferred rock flour declines sharply, consistent with rapid twentieth-century deglaciation. From the outermost LIA moraine crest to 1960 CE (USGS Anchorage B-6 topographic map), Eklutna Glacier has retreated ~1.8 km, and an additional ~2.5 km of retreat has occurred from 1960 to 2025 CE (Fig. 1C). The interpretation of PC1 during the 20th century deglaciation may be complicated by the construction of a water control structure in 1929 CE. Subsequent lake-level fluctuations, caused by winter drawdowns and summer refilling, have altered sedimentation patterns (Boes et al., 2018), potentially obscuring the natural sedimentation at core site EK14-1 following installation.

Thomas et al. (2021) used varve thickness in core EK14-2 as a proxy for glacier extent extending back to 2.3 ka. Their work identified two major glacier advances in the catchment, from 320 to 270 BCE and 1600–1900 CE. The first glacier advance is represented as a series of unusually thick varves at the base of EK14-2 around 2.3 ka and at the same time in Skilak Lake (SK16-2, Kenai Peninsula). In contrast, PC1 values from EK14-1 do not indicate a corresponding major increase in rock flour accumulation. Rather than a glacier advance, the thick basal varves in EK14-2 and SK16-2 may be the result of increased sediment accumulation rate related to lake level lowering, which can increase varve thickness during short time scales (Loso et al., 2004) or higher lake level, which eroded the shoreline and redistributed sediment to the core sites. Beach sand exposed in an outcrop along the northwestern shoreline of Eklutna Lake (Appendix A Section A2, Fig. A2) indicates that lake levels were up to ~7.0 m higher than the pre-dam lake level (259.1 m a.s.l.) at 2.2 ka. A shoreline at this elevation approximately coincides with the top of the moraine (~265 m a.s.l.) that naturally dams the lake. Undated shorelines as high as 304 m a.s.l. can be observed in high-resolution DEM of the valley wall east (~200 m) of Yuditna Creek (Fig. 2A; Dubé, 2022), further demonstrating that the pre-dam moraine could hold water above the modern full pool elevation. Furthermore, Thomas et al. (2021) noted that the elevated sediment accumulation rate at ~2.3 ka could reflect a multi-decadal interval of intensified rainfall or snowmelt runoff driven by a more easterly and strengthened Aleutian Low (Fig. 9A; Broadman et al., 2020b), which would have enhanced river sediment transport during this short-lived interval. Additionally, thicker intra-varve turbidite layers in the lake have been correlated with years of increased autumn precipitation (Boes et al., 2018), further suggesting that precipitation-driven runoff influences sediment delivery to the lake. However, in EK14-1, rather than coarsening as might be expected with higher discharge, grain sizes remain relatively stable over this interval (Fig. 3). Possibly, this relatively short-lived event, represented by a multi-decadal interval of thick varves, was not captured by our 40-year sampling interval.

PC1 from EK14-1 shows more multi-century variability between 270 BCE and 1600 CE than the varve thicknesses from EK14-2 and may be a better indicator of glacier fluctuations at Eklutna Lake. During this interval, EK14-2 and core SK16-2 from Skilak Lake contain consistently thin varves, which Thomas et al. (2021) interpreted as evidence that glaciers did not advance at either watershed over the ~1900-year period. In contrast, PC1 from EK14-1 indicates increasing rock flour (decreasing PC1 values) during the second half of the first millennium, which might coincide with the widely recognized First Millennium Advance (Reyes et al., 2006). During the last millennium, PC1 from core EK14-1 fluctuates on multi-century timescales, which contrasts with core EK14-2 varve thicknesses. Specifically, during the phases of the LIA, PC1 exhibits more multidecadal variability that is largely absent in the varve-thickness sequences. These PC1 fluctuations are consistent with evidence for multiple LIA advances, and they seem to coincide with solar minima, which generally track LIA glacier fluctuations in Alaska (Wiles et al., 2004, 2008), better than do varve thicknesses in core EK14-2 (Fig. 9F and G). Taken together, PC1 seems to provide a more accurate indicator of glacier fluctuations in the Eklutna Lake catchment over multi-century time scales than does varve thickness.

6. Conclusions

The 9.6 kyr sedimentary record from Eklutna Lake, combined with multivariate analyses of physical, chemical, and biological sediment indicators, comparisons with regional glacier chronologies and North Pacific paleoclimate records, demonstrates that:

1. **Integrated multi-proxy rock flour signal:** Although individual clastic (density, sedimentation rate, and particle size) and productivity indicators (BSi, OM, $RABD_{660;670}$) generally follow major Holocene climate transitions in Alaska, their centennial-to-millennial-scale offsets complicate the interpretation of a rock flour signal at Eklutna Lake. However, PCA of the EK14-1 dataset isolated the dominant, shared variance (PC1) that we interpret as a robust indicator of rock flour abundance and representative of glacier-size changes over time.
2. **Validating PC1 with other regional glacier change records:** Comparison of PC1 to periods of Holocene glacier expansion, stabilization, and climatic changes summarized in recent Alaska-wide reviews shows that the PC1 time series largely tracks previously published Holocene glacier and climate fluctuations.
3. **Early Holocene low lake level:** Shoreline regression during the early Holocene increased the proximity of sediment sources and coarse sediment deposition at core site EK14-1. The brown, coarse sediment and low sedimentation rate at the base of the core are distinctive, and its deposition aligns with regional evidence of lower lake levels until ~8.2 ka.
4. **Early Holocene glaciers:** Evidence for early Holocene rock flour input at Eklutna Lake is limited. PC1 indicates the lowest rock flour abundance of the entire sequence around 8.5 ka, suggesting that glaciers were at their smallest at this time.
5. **Reduced or absent glaciers:** PC1 values indicate consistently low rock flour abundance through 5.5 ka, and values stay below modern until ~4 ka. Consistent with regional evidence for reduced glacier extent under sustained warmth, glaciers were probably either absent or severely restricted to cirque areas until around 5.5 ka.
6. **Neoglacial advances:** PC1-inferred rock flour abundance shows several millennial-scale increases followed by a steady state, possibly correlated with moraine stabilization ages known from around Alaska. Glaciers reached near-modern limits by ~4 ka, as PC1 values at this time are similar to modern values.
7. **Common Era:** The time series of PC1 from core EK14-1 does not support the varve-thickness evidence for a prominent glacier advance around 2.3 ka (Thomas et al., 2021), which we now attribute to increased accumulation rate associated with high lake level. PC1 also exhibits more multidecadal variability than the varve sequences and displays peaks corresponding with two phases of the LIA coinciding with solar minima, which are largely absent in the varve-thickness records.

Author contributions

Hunter T. Allen: Conceptualization, Investigation, Formal analysis, Data Curation, Writing – original draft, Visualization. Darrell S. Kaufman: Conceptualization, Investigation, Project Administration, Resources, Writing – original draft, Supervision, Funding Acquisition. Nicholas P. McKay: Formal analysis, Resources, Writing – review & editing, Funding Acquisition. Erik Schiefer: Resources, Writing – review & editing. Laura J. Larocca: Writing – review & editing. Britta J. L. Jensen: Investigation, Writing – review & editing, Visualization. Matthew S. M. Bolton: Investigation, Writing – review & editing. Kathleen R. North: Investigation, Writing – review & editing. Nore Praet: Resources, Writing – review & editing. Maarten Van Daele: Resources, Writing – review & editing. Marc De Batist: Resources, Funding Acquisition, Writing – review & editing. Maurycy Żarczyński: Investigation, Writing – review & editing.

Declaration of competing interest

The authors declare that they have no known competing financial interests or personal relationships that could have appeared to influence the work reported in this paper.

Acknowledgements

We thank the following organizations and individuals: National Science Foundation (Award # 2303462), Research Foundation - Flanders (Grant #G042812N), and Polish National Agency for Academic Exchange (Project # BPN/BEK/2021/1/00133) for funding this research; Continental Scientific Drilling Facility, University of Minnesota for preliminary core analysis, XRF scanning, and travel support; Polar Field Services, Inc., for logistical support; Eklutna, Inc., for permission to access their land; Tracy Allen, Eli Allred, Mindy Bell, Ryan Ellis, and Monica Maynard, for field assistance; Jordon Bright, Leah Marshall and undergraduate researchers including: Cedar Bertelsen, Tatum Hardt, Joseph McDonald, Michelle Olichney, and Olivia Peretto for laboratory assistance; Jason Curtis, University of Florida for $CaCO_3$ analysis; Christopher Ebert NAU's ACE Isotope Laboratory for ^{14}C analysis; Jordon Bright and R. Scott Anderson, both at NAU, for identifying biogenic carbonates and macrofossils, respectively.

Appendix A. Supplementary text, figures and tables

Supplementary data to this article can be found online at https://doi.org/10.1016/j.quascirev.2026.110107.

Data availability

Appendix A includes all of the original data presented in this article. The dataset is also archived with the National Oceanic and Atmospheric Administration World Data Service for Paleoclimatology (NOAA/WDS-Paleo) at https://doi.org/10.25921/85yy-d321.

References

Aitchison, J., 1982. The statistical analysis of compositional data. J. R. Stat. Soc. Ser. B 44 (2), 139–177. https://doi.org/10.1111/j.2517-6161.1982.tb01195.x.

Alley, R.B., Cuffey, K.M., Zoet, L.K., 2019. Glacial erosion: status and outlook. Ann. Glaciol. 60, 1–13. https://doi.org/10.1017/aog.2019.38.

Anderson, R.S., Berg, E., Williams, C., Clark, T., 2019. Postglacial vegetation community change over an elevational gradient on the western Kenai Peninsula, Alaska: pollen records from Sunken Island and Choquette Lakes. J. Quat. Sci. 34, 309–322. https://doi.org/10.1002/jqs.3102.

Anderson, R.S., Hallett, D.J., Berg, E., Jass, R.B., Toney, J.L., De Fontaine, C.S., DeVolder, A., 2006. Holocene development of Boreal forests and fire regimes on the Kenai Lowlands of Alaska. Holocene 16, 791–803. https://doi.org/10.1191/0959683606hol966rp.

Auer, A.G., van der Bilt, W.G.M., Schomacker, A., Bakke, J., Støren, E.W.N., Buckby, J. M., Cederstrøm, J.M., van der Plas, S., 2025. Hydroclimate intensification likely aided glacier survival on Svalbard in the Early Holocene. Commun. Earth Environ. 6, 1–14. https://doi.org/10.1038/s43247-025-02064-z.

Bakke, J., Lie, Ø., Nesje, A., Dahl, S., Paasche, Ø., 2005a. Utilizing physical sediment variability in glacier-fed lakes for continuous glacier reconstructions during the Holocene, northern Folgefonna, western Norway. Holocene 15, 161–176. https://doi.org/10.1191/0959683605hl797rp.

Bakke, J., Dahl, S.O., Paasche, Ø., Løvlie, R., Nesje, A., 2005b. Glacier fluctuations, equilibrium-line altitudes and palaeoclimate in Lyngen, northern Norway, during the Lateglacial and Holocene. Holocene 15, 518–540. https://doi.org/10.1191/0959683605hl815rp.

Bakke, J., Trachsel, M., Kvisvik, B.C., Nesje, A., Lyså, A., 2013. Numerical analyses of a multi-proxy data set from a distal glacier-fed lake, Sørsendalsvatn, western Norway. Quat. Sci. Rev. 73, 182–195. https://doi.org/10.1016/j.quascirev.2013.05.003.

Balascio, N.L., D'Andrea, W.J., Bradley, R.S., 2015. Glacier response to North Atlantic climate variability during the Holocene. Clim. Past. 11 (12), 1587–1598. https://doi.org/10.5194/cp-11-1587-2015. https://cp.copernicus.org/articles/11/1587/2015/.

Barclay, D.J., Wiles, G.C., Calkin, P.E., 2009. Holocene glacier fluctuations in Alaska. Quat. Sci. Rev. 28, 2034–2048. https://doi.org/10.1016/j.quascirev.2009.01.016.

Benson, C.W., Kaufman, D.S., McKay, N.P., Schiefer, E., Fortin, D., 2019. A 16,000-yr-long sedimentary sequence from Lakes Peters and Schrader (Neruokpuk Lakes), northeastern Brooks Range, Alaska. Quat. Res. 92, 609–625. https://doi.org/10.1017/qua.2019.43.

Berg, E.E., Kaufman, D.S., Anderson, R.S., Wiles, G.C., Lowell, T.V., Mitchell, E.A.D., Hu, F.S., Werner, A., 2022. Late-Glacial and Holocene lake-level fluctuations on the Kenai Lowland, reconstructed from satellite-fen peat deposits and ice-shoved ramparts, Kenai Peninsula, Alaska. Quaternary 5, 23. https://doi.org/10.3390/quat5020023.

Bertrand, S., Tjallingii, R., Kylander, M.E., Wilhelm, B., Roberts, S.J., Arnaud, F., Brown, E., Bindler, R., 2024. Inorganic geochemistry of lake sediments: a review of analytical techniques and guidelines for data interpretation. Earth Sci. Rev. 249, 104639. https://doi.org/10.1016/j.earscirev.2023.104639.

Bird, B.W., Abbott, M.B., Finney, B.P., Kutchko, B., 2009. A 2000 year varve-based climate record from the central Brooks Range, Alaska. J. Paleolimnol. 41, 25–41. https://doi.org/10.1007/s10933-008-9262-y.

Blaauw, Maarten, Christen, J. Andrés, 2011. Flexible paleoclimate age-depth models using an autoregressive gamma process. Bayesian Anal. 6 (3). https://doi.org/10.1214/11-BA618.

Boes, E., Van Daele, M., Moernaut, J., Schmidt, S., Jensen, B.J.L., Praet, N., Kaufman, D., Haeussler, P., Loso, M.G., De Batist, M., 2018. Varve formation during the past three centuries in three large proglacial lakes in south-central Alaska. Geol. Soc. Am. Bull. 130, 757–774. https://doi.org/10.1130/B31792.1.

Bolton, M.S.M., Jensen, B.J.L., Wallace, K., Praet, N., Fortin, D., Kaufman, D., De Batist, M., 2020. Machine learning classifiers for attributing tephra to source volcanoes: an evaluation of methods for Alaska tephras. J. Quat. Sci. 35, 81–92. https://doi.org/10.1002/jqs.3170.

Brabets, T.P., 1993. Glacier Runoff and Sediment Transport and Deposition Eklutna Lake Basin, Alaska. Water-resources Investigation Report 92-4132. U.S. Department of the Interior. https://doi.org/10.3133/wri924132.

Broadman, E., Kaufman, D.S., Henderson, A.C.G., Berg, E.E., Anderson, R.S., Leng, M.J., Stahnke, S.A., Muñoz, S.E., 2020a. Multi-proxy evidence for millennial-scale changes in North Pacific Holocene hydroclimate from the Kenai Peninsula lowlands, south-central Alaska. Quat. Sci. Rev. 241, 106420. https://doi.org/10.1016/j.quascirev.2020.106420.

Broadman, E., Kaufman, D.S., Henderson, A.C.G., Malmierca-Vallet, I., Leng, M.J., Lacey, J.H., 2020b. Coupled impacts of sea ice variability and North Pacific atmospheric circulation on Holocene hydroclimate in Arctic Alaska. Proc. Natl. Acad. Sci. 117, 33034–33042. https://doi.org/10.1073/pnas.2016544117.

Butz, C., Grosjean, M., Fischer, D., Wunderle, S., Tylmann, W., Rein, B., 2015. Hyperspectral imaging spectroscopy: a promising method for the biogeochemical analysis of lake sediments. J. Appl. Remote Sens. 9, 096031. https://doi.org/10.1117/1.JRS.9.096031.

Church, M., Ryder, J.M., 1972. Paraglacial sedimentation: a consideration of fluvial processes conditioned by glaciation. Geol. Soc. Am. Bull. 83, 3059–3072. https://doi.org/10.1130/0016-7606(1972)83%255B3059:PSACOF%255D2.0.CO;2.

Clark, S.H.B, 1973. The McHugh Complex of south-central Alaska. U.S. Geological Survey Bulletin, pp. D1–D10. https://doi.org/10.3133/b1372d.

Clark, S.H.B., Bartsch, S.R., 1971. Reconnaissance Geologic Map and Geochemical Analyses of Stream Sediment and Rock Samples of the Anchorage B-6 Quadrangle. U. S. Geological Survey Open-File Report, Alaska. Report 71-70, 63 pp., 2 sheets, scale 1:63,360. https://doi.org/10.3133/mf351.

Combellick, R.A., Pinney, D.S., 1995. Radiocarbon age of probable Hayes Tephra, Kenai Peninsula, Alaska. Alaska Division of Geological & Geophysical Surveys, pp. 1–9. https://dx.doi.org/10.14509/2317.

Dahl, S.O., Bakke, J., Lie, Ø., Nesje, A., 2003. Reconstruction of former glacier equilibrium-line altitudes based on proglacial sites: an evaluation of approaches and selection of sites. Quat. Sci. Rev. 22, 275–287. https://doi.org/10.1016/S0277-3791(02)00135-X.

Daigle, T.A., Kaufman, D.S., 2009. Holocene climate inferred from glacier extent, lake sediment and tree rings at Goat Lake, Kenai Mountains, Alaska, USA. J. Quat. Sci. 24, 33–45. https://doi.org/10.1002/jqs.1166.

Davies, S.M., Albert, P.G., Bourne, A.J., Owen, S., Svensson, A., Bolton, M.S.M., Cook, E., Jensen, B.J.L., Jones, G., Ponomareva, V.V., Suzuki, T., 2024. Exploiting the Greenland volcanic ash repository to date caldera-forming eruptions and widespread isochrons during the Holocene. Quat. Sci. Rev. 334, 108707. https://doi.org/10.1016/j.quascirev.2024.108707.

Delaney, I., Adhikari, S., 2020. Increased subglacial sediment discharge in a warming climate: consideration of ice dynamics, glacial erosion, and fluvial sediment transport. Geophys. Res. Lett. 47. https://doi.org/10.1029/2019GL085672.

Desloges, J.R., 1994. Varve deposition and the sediment yield record at three small lakes of the southern Canadian Cordillera. Arct. Alp. Res. 26, 130–140. https://doi.org/10.2307/1551776.

Desloges, J.R., Gilbert, R., 1994. Sediment source and hydroclimatic inferences from glacial lake sediments: the postglacial sedimentary record of Lillooet Lake, British Columbia. J. Hydrol. 159, 375–393. https://doi.org/10.1016/0022-1694(94)90268-2.

Dietze, E., Dietze, M., 2019. Grain-size distribution unmixing using the R package EMMAgeo. E. G. Quatern. Sci. J. 68, 29–46. https://doi.org/10.5194/egqsj-68-29-2019.

Donovan, J.J., Kremser, D., Fournelle, J.H., Goemann, K., 2015. Probe for EPMA: Acquisition, Automation and Analysis, vol. 11. Probe Software Inc., Eugene, Oregon. http://www.probesoftware.com.

Douglas, M.S.V., Smol, J.P., 1999. Freshwater diatoms as indicators of environmental change in the High Arctic. In: Stoermer, E., Smol, J.P. (Eds.), The Diatoms: Applications for the Environment and Earth Sciences. Cambridge Univ. Press, Cambridge, U.K, pp. 227–244. https://doi.org/10.1017/CBO9780511763175.014.

Dubé, K.V., 2022. Eklutna Lake Project, Lakeside Trail Erosion Study, Study Report (DRAFT). Watershed GeoDynamics. https://eklutnahydro.com/wp-content/uploads/2022/06/2022-2-11-Eklutna-Study-Report_Lakeside-Trail-Erosion_DRAFT.pdf.

Ebisuzaki, W., 1997. A method to estimate the statistical significance of a correlation when the data are serially correlated. J. Clim. 10, 2147–2153. https://doi.org/10.1175/15200442(1997)010<2147:amtets>2.0.co;2.

Fang, L., Jenk, T.M., Winski, D., Kreutz, K., Brooks, H.L., Erwin, E., Osterberg, E., Campbell, S., Wake, C., Schwikowski, M., 2023. Early Holocene ice on the Begguya plateau (Mt. Hunter, Alaska) revealed by ice core ^{14} C age constraints. Cryosphere 17, 4007–4020. https://doi.org/10.5194/tc-17-4007-2023.

Fenn, C.R., 1987. Sediment transfer processes in alpine glacier basins. In: Gurnell, A.M., Clark, M.J. (Eds.), Glacio–Fluvial Sediment Transfer: an Alpine Perspective. Wiley, Chichester, pp. 59–85.

Fortin, D., Praet, N., McKay, N.P., Kaufman, D.S., Jensen, B.J.L., Haeussler, P.J., Buchanan, C., De Batist, M., 2019. New approach to assessing age uncertainties – the 2300-year varve chronology from Eklutna Lake, Alaska (USA). Quat. Sci. Rev. 203, 90–101. https://doi.org/10.1016/j.quascirev.2018.10.018.

Geck, J., Hock, R., Loso, M.G., Ostman, J., Dial, R., 2021. Modeling the impacts of climate change on mass balance and discharge of Eklutna Glacier, Alaska, 1985–2019. J. Glaciol. 67, 909–920. https://doi.org/10.1017/jog.2021.41.

Haeussler, P.J., Praet, N., Vandekerkhove, E., Vandorpe, T., Van Daele, M., De Rycker, K., Witter, R.C., Labay, K.A., Moernaut, J., De Batist, M., 2022. Gridded Data from Multibeam Bathymetric Surveys of Eklutna, Kenai, and Skilak Lakes. U.S. Geological Survey data release, Alaska. https://doi.org/10.5066/P9GK6YZG.

Hallet, B., Hunter, L., Bogen, J., 1996. Rates of erosion and sediment evacuation by glaciers: a review of field data and their implications. Glob. Planet. Change. 12, 213–235. https://doi.org/10.1016/0921-8181(95)00021-6.

Heusser, C.J., Heusser, L.E., Peteet, D.M., 1985. Late-Quaternary climatic change on the American North Pacific Coast. Nature 315, 485–487. https://doi.org/10.1038/315485a0.

Håkanson, L., Jansson, M., 1983. Principles of Lake Sedimentology. The Blackburn Press, Caldwell, NJ, USA, ISBN 978-3-642-69276-5. https://doi.org/10.1007/978-3-642-69274-1.

Hodgkins, R., 1999. Controls on suspended-sediment transfer at a high-arctic glacier, determined from statistical modelling. Earth Surf. Process. Landf. 24, 1–21. https://doi.org/10.1002/(SICI)1096-9837(199901)24:1%253C1::AID-ESP936%253E3.0.CO;2-P.

Jensen, B.J.L., Davies, L.J., Nolan, C., Pyne-O'Donnell, S., Monteath, A.J., Ponomareva, V., Portnyagin, M., Booth, R., Bursik, M., Cook, E., Plunkett, G., Vallance, J.W., Luo, Y., Cwynar, L.C., Hughes, P., Pearson, D.G., 2021. A latest Pleistocene and Holocene composite tephrostratigraphic framework for northeastern North America. Quat. Sci. Rev. 272, 107242. https://doi.org/10.1016/j.quascirev.2021.107242.

Jones, M.C., Peteet, D.M., Kurdyla, D., Guilderson, T., 2009. Climate and vegetation history from a 14,000-year peatland record, Kenai Peninsula, Alaska. Quat. Res. 72, 207–217. https://doi.org/10.1016/j.yqres.2009.04.002.

Karlén, W., 1976. Lacustrine sediments and tree-limit variations as indicators of Holocene climatic fluctuations in Lappland, Northern Sweden. Geogr. Ann. Phys. Geogr. 58, 1–34. https://doi.org/10.2307/520740.

Karlén, W., 1981. Lacustrine sediment studies. A technique to obtain a continuous record of Holocene glacier variations. Geogr. Ann. Phys. Geogr. 63, 273–281. https://doi.org/10.2307/520840.

Kaufman, D.S., Axford, Y.L., Henderson, A.C.G., McKay, N.P., Oswald, W.W., Saenger, C., Anderson, R.S., Bailey, H.L., Clegg, B., Gajewski, K., Hu, F.S., Jones, M.C., Massa, C., Routson, C.C., Werner, A., Wooller, M.J., Yu, Z., 2016. Holocene climate changes in eastern Beringia (NW North America) – a systematic review of multi-proxy evidence. Quat. Sci. Rev. 147, 312–339. https://doi.org/10.1016/j.quascirev.2015.10.021.

Kaufman, D.S., Sheng Hu, F., Briner, J.P., Werner, A., Finney, B.P., Gregory-Eaves, I., 2003. A ~33,000 year record of environmental change from Arolik Lake, Ahklun Mountains, Alaska, USA. J. Paleolimnol. 30, 343–361. https://doi.org/10.1023/B:JOPL.0000007219.15604.27.

Koerner, R.M., 2005. Mass balance of glaciers in the Queen Elizabeth Islands, Nunavut, Canada. Ann. Glaciol. 42, 417–423. https://doi.org/10.3189/172756405781813122.

Kuehn, S.C., Froese, D.G., Shane, P.A.R., 2011. The INTAV intercomparison of electron-beam microanalysis of glass by tephrochronology laboratories: results and recommendations. Quat. Int. 246, 19–47. https://doi.org/10.1016/j.quaint.2011.08.022.

LaBrecque, T.S., Kaufman, D.S., 2016. Holocene glacier fluctuations inferred from lacustrine sediment, Emerald Lake, Kenai Peninsula, Alaska. Quat. Res. 85, 34–43. https://doi.org/10.1016/j.yqres.2015.11.004.

Larocca, L.J., Axford, Y., Bjørk, A.A., Lasher, G.E., Brooks, J.P., 2020. Local glaciers record delayed peak Holocene warmth in south Greenland. Quat. Sci. Rev. 241, 106421. https://doi.org/10.1016/j.quascirev.2020.106421.

Larocca, L.J., Axford, Y., 2022. Arctic glaciers and ice caps through the Holocene: a circumpolar synthesis of lake-based reconstructions. Clim. Past 18, 579–606. https://doi.org/10.5194/cp-18-579-2022.

Lawson, D.E., 1993. Glaciohydrologic and glaciohydraulic effects on runoff and sediment yield in glacierized basins. US Army Corps Eng. Cold Reg. Res. Eng. Lab. Monogr. 93 (2), 108. https://apps.dtic.mil/sti/pdfs/ADA275134.pdf.

Leemann, A., Niessen, F., 1994. Holocene glacial activity and climatic variations in the Swiss Alps: reconstructing a continuous record from proglacial lake sediments. Holocene 4, 259–268. https://doi.org/10.1177/095968369400400305.

Lemmen, D.S., Gilbert, R., Smol, J.P., Hall, R.I., 1988. Holocene sedimentation in glacial Tasikutaaq Lake, Baffin Island. Can. J. Earth Sci. 25, 810–823. https://doi.org/10.1139/e88-080.

Lemot, F., Sabatier, P., Chevalier, M.-L., Crouzet, C., Kermagoret, L., Rioual, P., Bai, M., Jacq, K., Findling, N., Replumaz, A., 2024. Proglacial lake response to late-holocene glacial fluctuations in southeast Tibet. Global Planet. Change 232, 104347. https://doi.org/10.1016/j.gloplacha.2023.104347.

Leonard, E.M., 1997. The relationship between glacial activity and sediment production: evidence from a 4450-year varve record of neoglacial sedimentation in Hector Lake, Alberta, Canada. J. Paleolimnol. 17, 319–330. https://doi.org/10.1023/A:1007948327654.

Leonard, E.M., Reasoner, M.A., 1999. A continuous Holocene glacial record inferred from proglacial lake sediments in Banff National Park, Alberta, Canada. Quat. Res. 51, 1–13. https://doi.org/10.1006/qres.1998.2009.

Levy, L.B., Kaufman, D.S., Werner, A., 2004. Holocene glacier fluctuations, Waskey Lake, northeastern Ahklun Mountains, southwestern Alaska. Holocene 14, 185–193. https://doi.org/10.1191/0959683604hl675rp.

Loso, M.G., 2009. Summer temperatures during the Medieval Warm Period and Little Ice Age inferred from varved proglacial lake sediments in southern Alaska. J. Paleolimnol. 41, 117–128. https://doi.org/10.1007/s10933-008-9264-9.

Loso, M.G., Anderson, R.S., Anderson, S.P., 2004. Post–Little Ice Age record of coarse and fine clastic sedimentation in an Alaskan proglacial lake. Geol. 32, 1065. https://doi.org/10.1130/G20839.1.

Matthews, J.A., Olaf Dahl, S., Nesje, A., Berrisford, M.S., Andersson, C., 2000. Holocene glacier variations in central Jotunheimen, southern Norway based on distal glaciolacustrine sediment cores. Quat. Sci. Rev. 19, 1625–1647. https://doi.org/10.1016/S0277-3791(00)00008-1.

McDonald, T., Briner, J.P., 2026. Latest Pleistocene and Holocene local glacial history of Baranof Island, southeast Alaska. Quat. Res. 1–18. https://doi.org/10.1017/qua.2026.10079.

McKay, N.P., Kaufman, D.S., 2009. Holocene climate and glacier variability at Hallet and Greyling Lakes, Chugach Mountains, south-central Alaska. J. Paleolimnol. 41, 143–159. https://doi.org/10.1007/s10933-008-9260-0.

McKay, Nicholas P., Emile-Geay, Julien, 2016. Technical note: The Linked Paleo Data framework – a common tongue for paleoclimatology. Clim. Past 12 (4), 1093–1100. https://doi.org/10.5194/cp-12-1093-2016. https://cp.copernicus.org/articles/12/1093/2016/.

McKay, N.P., Kaufman, D.S., Michelutti, N., 2008. Biogenic silica concentration as a high-resolution, quantitative temperature proxy at Hallet Lake, south-central Alaska. Geophys. Res. Lett. 35. https://doi.org/10.1029/2007GL032876.

McKay, N.P., Kaufman, D.S., Routson, C.C., Erb, M.P., Zander, P.D., 2018. The onset and rate of Holocene Neoglacial cooling in the Arctic. Geophys. Res. Lett. 45 (12), 487–496. https://doi.org/10.1029/2018GL079773.

McKay, N.P., Emile-Geay, J., Khider, D., 2021. geoChronR – an R package to model, analyze, and visualize age-uncertain data. Geochronology 3, 149–169. https://doi.org/10.5194/gchron-3-149-2021.

Mortlock, R.A., Froelich, P.N., 1989. A simple method for the rapid determination of biogenic opal in pelagic marine sediments. Deep-Sea Res. 36, 1415–1426. https://doi.org/10.1016/0198-0149(89)90092-7.

Nesje, A., Olaf Dahl, S., Andersson, C., Matthews, J.A., 2000. The lacustrine sedimentary sequence in Sygneskardvatnet, western Norway: a continuous, high-resolution record of the Jostedalsbreen ice cap during the Holocene. Quat. Sci. Rev. 19, 1047–1065. https://doi.org/10.1016/S0277-3791(99)00090-6.

Noon, P.E., Birks, H.J.B., Jones, V.J., Ellis-Evans, J.C., 2001. Quantitative models for reconstructing catchment ice-extent using physical-chemical characteristics of lake sediments. J. Paleolimnol. 25, 375–392. https://doi.org/10.1023/A:1011193401627.

Norris, S.L., Gosse, J.C., Millan, R., Mouginot, J., Rabatel, A., Morlighem, M., Bolton, M. S.M., Alley, R.B., 2025. Drivers of global glacial erosion rates. Nat. Geosci. 18, 732–739. https://doi.org/10.1038/s41561-025-01747-8.

Oerlemans, J., 2005. Extracting a climate signal from 169 glacier records. Science 308, 675–677. https://doi.org/10.1126/science.1107046.

Olsson, I., 1986. Radiometric methods. In: Berglund, B. (Ed.), Handbook of Holocene Palaeoecology and Palaeohydrology. John Wiley & Sons, Chichester, pp. 273–312.

Overland, J.E., Adams, J.M., Bond, N.A., 1999. Decadal variability of the Aleutian Low and its relation to high-latitude circulation. J. Clim. 12 (5), 1542–1548. https://doi.org/10.1175/1520-0442(1999)012%3C1542:DVOTAL%3E2.0.CO;2.

Porter, C., Howat, I., Noh, M.J., Husby, E., Khuvis, S., Danish, E., Tomko, K., Gardiner, J., Negrete, A., Yadav, B., Klassen, J., Kelleher, C., Cloutier, M., Bakker, J., Enos, J., Arnold, G., Bauer, G., Morin, P., 2023. ArcticDEM - mosaics. Harvard Dataverse V1. https://doi.org/10.7910/DVN/3VDC4W.

Praet, N., Moernaut, J., Daele, M.V., Boes, E., Haeussler, P.J., Strupler, M., Schmidt, S., Loso, M.G., Batist, M.D., 2017. Paleoseismic potential of sublacustrine landslide records in a high-seismicity setting (South-central Alaska). Mar. Geol. 384, 103–119. https://doi.org/10.1016/j.margeo.2016.05.004.

Praet, N., Van Daele, M., Collart, T., Moernaut, J., Vandekerkhove, E., Kempf, P., Haeussler, P.J., De Batist, M., 2020. Turbidite stratigraphy in proglacial lakes: deciphering trigger mechanisms using a statistical approach. Sedimentology 67, 2332–2359. https://doi.org/10.1111/sed.12703.

Praet, N., Van Daele, M., Moernaut, J., Mestdagh, T., Vandorpe, T., Jensen, B.J.L., Witter, R.C., Haeussler, P.J., De Batist, M., 2022. Unravelling a 2300 year long sedimentary record of megathrust and intraslab earthquakes in proglacial Skilak Lake, south-central Alaska. Sedimentology 69, 2151–2180. https://doi.org/10.1111/sed.12986.

Praet, N., Van Daele, M., Wils, K., Haeussler, P.J., Witter, R.C., McKay, N.P., Jensen, B.J. L., Moernaut, J., De Batist, M., 2025. Refining the earthquake history of south-central Alaska through lake records. Earth Sci. Rev., 105249 https://doi.org/10.1016/j.earscirev.2025.105249.

Reimer, P.J., Austin, W.E.N., Bard, E., Bayliss, A., Blackwell, P.G., Bronk Ramsey, C., Butzin, M., Cheng, H., Edwards, R.L., Friedrich, M., Grootes, P.M., Guilderson, T.P., Hajdas, I., Heaton, T.J., Hogg, A.G., Hughen, K.A., Kromer, B., Manning, S.W., Muscheler, R., Palmer, J.G., Pearson, C., van der Plicht, J., Reimer, R.W., Richards, D.A., Scott, E.M., Southon, J.R., Turney, C.S.M., Wacker, L., Adolphi, F., Büntgen, U., Capano, M., Fahrni, S.M., Fogtmann-Schulz, A., Friedrich, R., Köhler, P., Kudsk, S., Miyake, F., Olsen, J., Reinig, F., Sakamoto, M., Sookdeo, A., Talamo, S., 2020. The IntCal20 Northern Hemisphere radiocarbon age calibration curve (0–55 cal kBP). Radiocarbon 62, 725–757. https://doi.org/10.1017/RDC.2020.41.

Reimer, P.J., Bard, E., Bayliss, A., Beck, J.W., Blackwell, P.G., Ramsey, C.B., Buck, C.E., Cheng, H., Edwards, R.L., Friedrich, M., Grootes, P.M., Guilderson, T.P., Haflidason, H., Hajdas, I., Hatté, C., Heaton, T.J., Hoffmann, D.L., Hogg, A.G., Hughen, K.A., Kaiser, K.F., Kromer, B., Manning, S.W., Niu, M., Reimer, R.W., Richards, D.A., Scott, E.M., Southon, J.R., Staff, R.A., Turney, C.S.M., Plicht, J. van der, 2013. IntCal13 and Marine13 radiocarbon age calibration curves 0–50,000 years cal BP. Radiocarbon 55, 1869–1887. https://doi.org/10.2458/azu_js_rc.55.16947.

Rein, B., Sirocko, F., 2002. In-situ reflectance spectroscopy-analyzing techniques for high resolution pigment logging in sediment cores. Int. J. Earth Sci. 91, 950–954. https://doi.org/10.1007/s00531-002-0264-0.

Reyes, A.V., Wiles, G.C., Smith, D.J., Barclay, D.J., Allen, S., Jackson, S., Larocque, S., Laxton, S., Lewis, D., Calkin, P.E., Clague, J.J., 2006. Expansion of alpine glaciers in Pacific North America in the first millennium A. D. Geology 34, 57–60. https://doi.org/10.1130/G21902.1.

RGI 7.0 Consortium, 2023. Randolph Glacier Inventory - a Dataset of Global Glacier Outlines, Version 7.0. NSIDC: National Snow and Ice Data Center, Boulder, Colorado USA. https://doi.org/10.5067/f6jmovy5navz.

Rose, K.C., Hamilton, D.P., Williamson, C.E., McBride, C.G., Fischer, J.M., Olson, M.H., Saros, J.E., Allan, M.G., Cabrol, N., 2014. Light attenuation characteristics of glacially-fed lakes. J. Geophys. Res. Biogeosci. 119, 1446–1457. https://doi.org/10.1002/2014JG002674.

Rosenbaum, J.G., Reynolds, R.L., 2004. Record of Late Pleistocene glaciation and deglaciation in the Southern Cascade Range. II. Flux of glacial flour in a sediment core from Upper Klamath Lake, Oregon. J. Paleolimnol. 31, 235–252. https://doi.org/10.1023/B:JOPL.0000019229.75336.7a.

Røthe, T., Bakke, J., Vasskog, K., Gjerde, M., D'Andrea, W., Bradley, R., 2015. Arctic Holocene glacier fluctuations reconstructed from lake sediments at Mitrahalvøya, Spitsbergen. Quat. Sci. Rev. 109, 111–125. https://doi.org/10.1016/j.quascirev.2014.11.017.

Sass, L.C., Loso, M.G., Geck, J., Thoms, E.E., Mcgrath, D., 2017. Geometry, mass balance and thinning at Eklutna Glacier, Alaska: an altitude-mass-balance feedback with implications for water resources. J. Glaciol. 63, 343–354. https://doi.org/10.1017/jog.2016.146.

Sauvageau, C., Schult, D., 2022. Eklutna Hydroelectric Project Water Quality Year 1 Interim Report. McMillen Jacobs Associates. https://eklutnahydro.com/wp-content/uploads/2022/06/2022-2-11-Eklutna-Year-1-Interim-Report_Water-Quality_DRAFT.pdf.

Sauvageau, C., Schult, D., 2023. Eklutna Hydroelectric Project Water Quality Year 2 Study Report. McMillen Jacobs Associates. https://eklutnahydro.com/wp-content/uploads/2023/06/Eklutna-Water-Quality-Y2-Report_FINAL.pdf.

Schiefer, E., Geck, J., Ostman, J.S., McKay, N.P., Praet, N., Loso, M.G., Kaufman, D.S., 2021. Fluvial suspended sediment transfer and lacustrine sedimentation of recent flood turbidites in proglacial Eklutna Lake, western Chugach Mountains, Alaska. Hydrol. Process. 35, e14375. https://doi.org/10.1002/hyp.14375.

Schiefer, E., Gilbert, R., 2008. Proglacial sediment trapping in recently formed Silt Lake, upper Lillooet Valley, Coast Mountains, British Columbia. Earth Surf. Process. Landf. 33, 1542–1556. https://doi.org/10.1002/esp.1625.

Schmoll, H.R., Yehle, L.A., Updike, R.G., 1999. Summary of Quaternary geology of the Municipality of Anchorage, Alaska. Quat. Int. 60, 3–36. https://doi.org/10.1016/S1040-6182(99)00004-X.

Smith, N.D., Ashley, G., 1985. Proglacial lacustrine environment. In: Ashley, G.M., Shaw, J., Smith, N.D. (Eds.), Glacial Sedimentary Environments. SEPM Society for Sedimentary Geology, pp. 135–215. https://doi.org/10.2110/scn.85.02.0135.

Solomina, O.N., Bradley, R.S., Hodgson, D.A., Ivy-Ochs, S., Jomelli, V., Mackintosh, A.N., Nesje, A., Owen, L.A., Wanner, H., Wiles, G.C., Young, N.E., 2015. Holocene glacier fluctuations. Quat. Sci. Rev. 111, 9–34. https://doi.org/10.1016/j.quascirev.2014.11.018.

Solomina, O.N., Bradley, R.S., Jomelli, V., Geirsdottir, A., Kaufman, D.S., Koch, J., McKay, N.P., Masiokas, M., Miller, G., Nesje, A., Nicolussi, K., Owen, L.A., Putnam, A.E., Wanner, H., Wiles, G., Yang, B., 2016. Glacier fluctuations during the past 2000 years. Quat. Sci. Rev. 149, 61–90. https://doi.org/10.1016/j.quascirev.2016.04.008.

Stacklies, W., Redestig, H., Scholz, M., Walther, D., Selbig, J., 2007. pcaMethods – a Bioconductor package providing PCA methods for incomplete data. Bioinformatics 23 (9), 1164–1167. https://doi.org/10.1093/bioinformatics/btm069.

Stansell, N.D., Rodbell, D.T., Abbott, M.B., Mark, B.G., 2013. Proglacial lake sediment records of Holocene climate change in the western Cordillera of Peru. Quat. Sci. Rev. 70, 1–14. https://doi.org/10.1016/j.quascirev.2013.03.003.

Stuiver, M., Reimer, P.J., 1993. Extended ^{14}C database and revised CALIB 3.0 ^{14}C Age Calibration Program. Radiocarbon 35, 215–230. https://doi.org/10.1017/S0033822200013904.

Thomas, J.E., Kaufman, D.S., Praet, N., McKay, N.P., Van Daele, M., Jensen, B.J.L., De Batist, M., 2021. A 2300-year record of glacier fluctuations at Skilak and Eklutna Lakes, south-central Alaska. Quat. Sci. Rev. 272, 107215. https://doi.org/10.1016/j.quascirev.2021.107215.

Tipping, M.E., Bishop, C.M., 1999. Probabilistic principal component analysis. J. Roy. Stat. Soc. B 61, 611–622. https://doi.org/10.1111/1467-9868.00196.

Updike, R.G., Ulery, C.A., 1983. Preliminary Geologic Map of the Anchorage B-6 NW (Eklutna Lake) Quadrangle, vols. 83–8. Alaska Division of Geological & Geophysical Surveys Report of Investigation, Alaska, 2 sheets, scale 1:10,000. https://doi.org/10.14509/2347.

Vail, P.R., Mitchum Jr., R.M., Thompson III, S., 1977. Seismic stratigraphy and global changes of sea level, part 3: relative changes of sea level from coastal onlap. In: Payton, C.E. (Ed.), Seismic Stratigraphy — Applications to Hydrocarbon Exploration, vol. 26. AAPG Memoir, pp. 63–81. https://doi.org/10.1306/M26490C5.

Valentino, J.D., Owen, L.A., Spotila, J.A., Cesta, J.M., Caffee, M.W., 2021. Timing and extent of late Pleistocene glaciation in the Chugach Mountains, Alaska. Quat. Res. 101, 205–224. https://doi.org/10.1017/qua.2020.106.

Van Daele, M., Haeussler, P.J., Witter, R.C., Praet, N., De Batist, M., 2020. The Sedimentary Record of the 2018 Anchorage earthquake in Eklutna Lake, Alaska: calibrating the lacustrine seismograph. Seismol. Res. Lett. 91, 126–141. https://doi.org/10.1785/0220190204.

Vandekerkhove, E., Van Daele, M., Praet, N., Cnudde, V., Haeussler, P.J., De Batist, M., 2020. Flood-triggered versus earthquake-triggered turbidites: a sedimentological study in clastic lake sediments (Eklutna Lake, Alaska). Sedimentology 67, 364–389. https://doi.org/10.1111/sed.12646.

Vasskog, K., Paasche, Ø., Nesje, A., Boyle, J.F., Birks, H.J.B., 2012. A new approach for reconstructing glacier variability based on lake sediments recording input from more than one glacier. Quat. Res. 77, 192–204. https://doi.org/10.1016/j.yqres.2011.10.001.

Wallace, K, Coombs, ML, Hayden, LA, Waythomas, CF, 2014. U.S. Geological Survey Scientific Investigations Report. USGS SIR 2014-5133. https://pubs.usgs.gov/sir/2014/5133/pdf/sir2014-5133.pdf.

Weltje, G.J., Bloemsma, M.R., Tjallingii, R., Heslop, D., Röhl, U., et al., 2015. Prediction of geochemical composition from XRF core scanner data: A new multivariate approach including automatic selection of calibration samples and quantification of uncertainties. Dev. Paleoenviron. Res. Springer Netherlands, Dordrecht, ISBN 9789401798488, pp. 507–534. https://doi.org/10.1007/978-94-017-9849-5_21. https://link.springer.com/10.1007/978-94-017-9849-5_21.

Werder, M.A., Hewitt, I.J., Schoof, C.G., Flowers, G.E., 2013. Modeling channelized and distributed subglacial drainage in two dimensions. J. Geophys. Res. Earth Surf. 118, 2140–2158. https://doi.org/10.1002/jgrf.20146.

Wiles, G.C., D'Arrigo, R.D., Villalba, R., Calkin, P.E., Barclay, D.J., 2004. Century-scale solar variability and Alaskan temperature change over the past millennium. Geophys. Res. Lett. 31 (13). https://doi.org/10.1029/2004GL020050.

Wiles, G.C., Barclay, D.J., Calkin, P.E., Lowell, T.V., 2008. Century to millennial-scale temperature variations for the last two thousand years indicated from glacial geologic records of Southern Alaska. Glob. Planet. Change. 60, 115–125. https://doi.org/10.1016/j.gloplacha.2006.07.036.

Winkler, G.R., 1992. Geologic map and summary geochronology of the Anchorage 1 degree x 3 degrees Quadrangle, southern Alaska. IMAP 2283. U.S. Geological Survey, Geologic Investigations Series Map. https://doi.org/10.3133/i2283, 1992.

Wittmeier, H.E., Bakke, J., Vasskog, K., Trachsel, M., 2015. Reconstructing Holocene glacier activity at Langfjordjøkelen, Arctic Norway, using multi-proxy fingerprinting of distal glacier-fed lake sediments. Quat. Sci. Rev. 114, 78–99. https://doi.org/10.1016/j.quascirev.2015.02.007.

Wolfe, A.P., Vinebrooke, R.D., Michelutti, N., Rivard, B., Das, B., 2006. Experimental calibration of lake-sediment spectral reflectance to chlorophyll a concentrations: methodology and paleolimnological validation. J. Paleolimnol. 36, 91–100. https://doi.org/10.1007/s10933-006-0006-6.

Wrobleski, E.A., Broadman, E., Werner, A., Rodbell, D.T., Kaufman, D.S., 2023. Postglacial environmental change inferred from carbonate- and organic-rich sediments of groundwater-fed Kelly Lake, Kenai Peninsula, south-central Alaska. J. Quat. Sci. 38, 1233–1250. https://doi.org/10.1002/jqs.3550.

Xiao, J., Chang, Z., Si, B., Qin, X., Itoh, S., Lomtatidze, Z., 2009. Partitioning of the grain-size components of Dali Lake core sediments: evidence for lake-level changes during the Holocene. J. Paleolimnol. 42, 249–260. https://doi.org/10.1007/s10933-008-9274-7.

Yu, Z., Walker, K.N., Evenson, E.B., Hajdas, I., 2008. Lateglacial and early Holocene climate oscillations in the Matanuska Valley, south-central Alaska. Quat. Sci. Rev. 27, 148–161. https://doi.org/10.1016/j.quascirev.2007.02.020.

Zander, P.D., Kaufman, D.S., McKay, N.P., Kuehn, S.C., Henderson, A.C.G., 2018. Using correlated tephras to refine radiocarbon-based age models, upper and lower Whitshed Lakes, south-central Alaska. Quat. Geochronol. 45, 9–22. https://doi.org/10.1016/j.quageo.2018.01.005.

Zander, P.D., Szidat, S., Kaufman, D.S., Żarczyński, M., Poraj-Górska, A.I., Boltshauser-Kaltenrieder, P., Grosjean, M., 2020. Miniature radiocarbon measurements (< 150 μg C) from sediments of Lake Żabińskie, Poland: effect of precision and dating density on age–depth models. Geochronology 2, 63–79. https://doi.org/10.5194/gchron-2-63-2020.